

Research



Cite this article: Torres-Ulloa C, Grassia P.

2021 Breakdown of similarity solutions: a perturbation approach for front propagation during foam-improved oil recovery. *Proc. R. Soc. A* **477**: 20200691.

<https://doi.org/10.1098/rspa.2020.0691>

Received: 26 August 2020

Accepted: 17 December 2020

Subject Areas:

applied mathematics, chemical engineering, fluid mechanics

Keywords:

pressure-driven growth model, foams, front propagation, porous media, Taylor expansion

Author for correspondence:

Carlos Torres-Ulloa

e-mail: carlos.torres-ulloa@strath.ac.uk;

carlos.torres@uct.cl

Electronic supplementary material is available online at <https://doi.org/10.6084/m9.figshare.c.5273531>.

Breakdown of similarity solutions: a perturbation approach for front propagation during foam-improved oil recovery

Carlos Torres-Ulloa^{1,2} and Paul Grassia¹

¹Department of Chemical and Process Engineering, University of Strathclyde, James Weir Building, 75 Montrose Street, Glasgow G1 1XJ, UK

²Departamento de Procesos Industriales, Facultad de Ingeniería, Universidad Católica de Temuco, Av. Rudecindo Ortega 02950, Temuco, Chile

CT-U, 0000-0003-4165-1339; PG, 0000-0001-5236-1850

The pressure-driven growth model has been employed to study a propagating foam front in the foam-improved oil recovery process. A first-order solution of the model proves the existence of a concave corner on the front, which initially migrates downwards at a well defined speed that differs from the speed of front material points. At later times, however, it remains unclear how the concave corner moves and interacts with points on the front either side of it, specifically whether material points are extracted from the corner or consumed by it. To address these questions, a second-order solution is proposed, perturbing the aforementioned first-order solution. However, the perturbation is challenging to develop, owing to the nature of the first-order solution, which is a similarity solution that exhibits strong spatio-temporal non-uniformities. The second-order solution indicates that the corner's vertical velocity component decreases as the front migrates and that points initially extracted from the front are subsequently consumed by it. Overall, the perturbation approach developed herein demonstrates how early-time similarity solutions exhibiting strong spatio-temporal non-uniformities break down as time proceeds.

1. Introduction

Foam applications occur in several industrial processes, such as mining, food and cosmetics, production of glass, foam fractionation, firefighting, as well in medicine, in a process known as foam sclerotherapy [1–3]. Specifically, what is studied in the present work is an application that involves foam flow through porous media, such as soil remediation and foam-improved oil recovery (foam IOR) [4–6]. In those processes, the foam is used to sweep or remove a specific material, be it a pollutant or a valuable component from the porous media [7–9]. In petroleum engineering applications, during the oil recovery process, typically up to a third of the oil originally present in the reservoir is recovered after the primary and secondary stages of extraction [4]. Then, a set of techniques known as enhanced or improved oil recovery can be employed to recover the additional remaining oil from the porous media [5]. In particular, foam IOR is a tertiary oil extraction technique that consists of the injection of gas into the reservoir (figure 1) after the deposit has been flooded with a surfactant solution [5]. Upon contacting the surfactant, the gas generates foam, which propagates pushing the liquid (oil and surfactant solution) to the extraction well (figure 1). The process relies on the foam films that are formed being stable enough to survive as they propagate through the porous medium, displacing reservoir liquids ahead of them. Stability of propagating foam films in the presence of oil can be challenging, although surfactant formulations can be found that, for particular oil types, impart good stability to the films [14–18].

(a) Foam in porous media

Modelling how foam propagates inside the reservoir is of great interest, since we cannot see what is happening underground. Fortunately, there have been numerous studies of the mechanisms by which foam is generated within and propagates within porous media [5,10,19–26], so insights into the elements that are required within a model are available. In porous media, foam films can severely restrict the motion of gas; the gas mobility falls due to the presence of foam films blocking the flow paths of gas [22]. Further upstream where foam is drier, foam films undergo capillary collapse. Upstream then, even though foam films might be present blocking certain pores, if there are sufficient unblocked pores so that gas is able to find a flow path, then mobility is much higher. Hence, what restricts motion is the zone of finely textured foam where injected gas meets liquids already in the reservoir [27], not drier and coarser foam upstream or unfoamed reservoir liquids downstream [12,22]. Therefore, we can track the front propagation by considering just the region where foam is being generated. The thickness of this region, compared with other length scales, i.e. the depth to which the foam penetrates, and the trajectory through which the front has moved, is relatively small, such that it can be considered as a sharp propagation front (a curve with negligible thickness) [10,27]. Hence, the front itself consists of the zone of finely textured foam, separating (as mentioned above) coarsely textured, collapsed foam upstream from liquids (surfactant solution and oil) downstream. Foam in porous media is of course a rheologically complex fluid (which among other things) can exhibit shear thinning behaviour [19,22,25,28–30]. For the purposes to be considered here though, what matters is that at the front, we have a finely textured foam, which has very low mobility. The total fluid mobility either side of the front is substantially larger than that at the front itself, possibly by as much as four orders of magnitude [12,29], so that it is possible to consider that all the pressure drop occurs across the propagating front, where the entire dynamics is focused [27]. Consequently, the front is pushed along the reservoir by pressure and at the same time is retarded by dissipation across the finely textured foam zone, with the width of this zone gradually increasing with time (as follows from fractional flow theory) but always remaining thin relative to front displacement [10]. As the front motion is driven by the pressure difference across it, its velocity decreases with depth, since the injection pressure behind remains fixed, but the hydrostatic pressure ahead increases with the depth. Therefore, there is a maximum depth (used to non-dimensionalize length scales in the system) to which the foam can penetrate, i.e. the depth at which the injected gas pressure equals

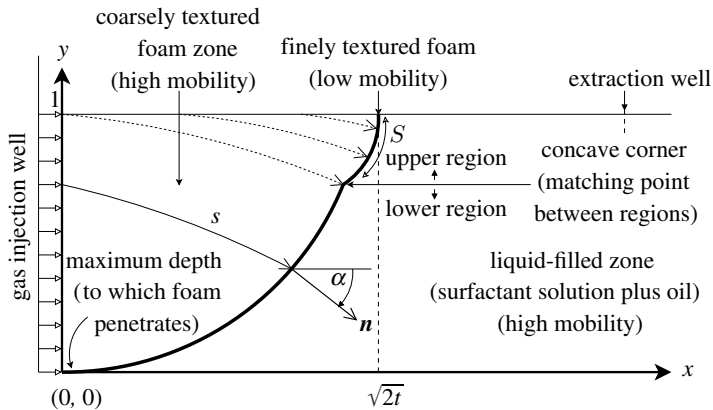


Figure 1. Definition sketch: Foam front propagation across a vertical domain $y \in [0, 1]$ and a horizontal domain $x \in [0, \infty)$. Variables are non-dimensionalized as established in refs. [5,10,11]. Here, S is the distance along the front measured downward. The foam is created by the injection of gas, forming a finely textured zone of small thickness at the propagating foam front. The front is represented here by a solid curve, which is vertically divided into two regions, separated by a concave corner, and this concave corner being the matching point between an upper and a lower region. Furthermore, the propagation front itself divides the reservoir into two zones: the coarsely textured foam (to the left) and the liquid-filled zone (to the right). Both of these zones have much higher mobility than the propagation front [5,12,13]. Locally, each point on the front moves in the normal \mathbf{n} direction, which is at an angle α from the horizontal (each point following its own trajectory of length s). The trajectory that has been followed by the points constituting the upper region is drawn with dotted lines, originating at the top boundary, those points having been injected from the top and hence having been part of the front, during less time than the original ones (present from $t = 0$, trajectories drawn with solid line) that constitute the lower region. At the top of the front ($y = 1$), the front position as a function of time is $\sqrt{2t}$ (in dimensionless variables) [10], which will be employed in this work as a top boundary condition.

the hydrostatic pressure [27]. This maximum depth scales proportionally to gas injection pressure and inversely with liquid–gas density difference and gravitational acceleration. Far above this maximum depth, however, the front is known to exhibit a concave corner or kink [27] (figure 1), which starts off right at the top and migrates downward. Determining how this concave corner moves is the issue addressed in this work.

(b) Concave corner and spatio-temporal non-uniformities

Physically, the concave corner or kink corresponds to an abrupt reorientation of the front over a limited length scale. A locally non-smooth front shape, such as this concave corner represents, may induce fingering phenomena, which decrease the process efficiency [10], thereby highlighting the importance of identifying its position. Mathematically, the concave corner arises due to an incompatibility when trying to match material points that have been on the propagation front since the start of the injection process (all found in the so-called lower region below the corner) and material points that have been newly injected from the top boundary since the initial time (the so-called upper region) [27] (figure 2). The position of the kink/corner can be tracked over time (see e.g. §4) in terms of ‘similarity variables’ at early times [27]. Early time here means small compared with the characteristic time scale identified in ref. [10], which is used to make the system dimensionless. This time scale turns out to be proportional to the following quantities: gas saturation at the front, porosity of the medium, maximum penetration depth squared and the (assumed roughly constant, based on fractional flow theory) ratio between front thickness and front displacement, and inversely proportional to medium permeability, relative mobility of foamed gas and pressure used to drive the foam. A typical value of this time scale has been estimated as around 11–14 days [21,31]. However, the important point for the current work is that this time scale is defined such that, at dimensionless time $t = 1/2$, the front is displaced

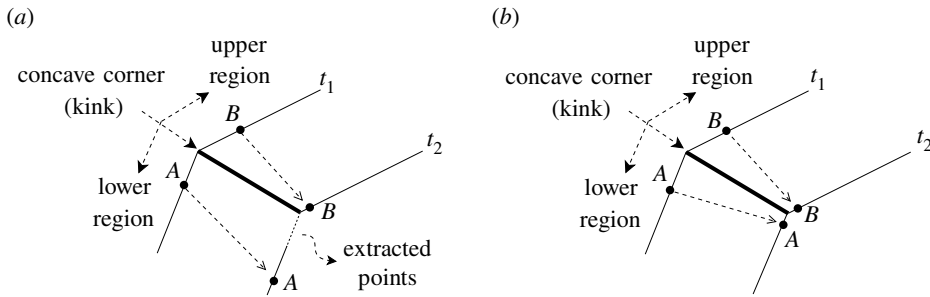


Figure 2. Possible trajectories of material points in the neighbourhood of the kink or concave corner. (a) Points between the fixed material point A and the kink move away from it, opening a gap between times t_1 and t_2 . This gap is filled by points extracted from the kink. Points between the fixed material point B and the kink are consumed between times t_1 and t_2 . (b) An alternative scenario where points between fixed material points A and B , and the kink/corner, are consumed over a time interval between t_1 and t_2 .

horizontally by an amount equal to its maximum penetration depth [10]. Small time therefore means the top of the front is displaced horizontally by much less than the depth over which the front is displaced overall.

Using the similarity solution, a first-order approximation to the location of the concave corner or kink was found [27]. However, as time proceeds, the first-order similarity solution deviates from a numerical and therefore more exact solution [32]. This first-order solution showed the corner moving downwards (at very early times) more slowly than the second-order approximation to the material point initially at the top of the lower region, which meant that new material points were being extracted from the kink or corner to populate the lower region (figure 2a). Nevertheless, given that the second-order approximation to the point initially at the top of the lower region indicates that material point's vertical motion slows down over time, eventually it is overtaken by the first-order approximation to the corner or kink: material points in the lower region are now being consumed by the kink not extracted from it (figure 2b). In this context, extracting material points implies physically that the zone of finely textured foam would need to thin slightly (at least temporarily), whereas consuming/destroying such points implies that this region must thicken a little (again at least temporarily). These are just temporary effects, since away from the corner, a local balance between microscale foam generation and foam destruction mechanisms quickly restores the thickness of the finely textured zone to its previous value (i.e. front thickness proportional to front displacement as mentioned above) on time scales much shorter than the total time for which the front propagates [30]. It is not clear, however, whether this prediction of material points being extracted/consumed is the actual behaviour or merely an artefact of having a second-order approximation for one quantity (the material point) and a first-order approximation for the other (the corner). The aim of this article then is to obtain the second-order approximation to the corner or kink location by improving upon the first-order solution in the upper region. The question we address then is whether a transition is still seen between the scenario of figure 2a and that of figure 2b when a consistent second-order approximation is used. Obtaining a second-order solution in the upper region is however challenging, more so than obtaining second-order solutions in the lower region was [27]. Indeed, given that the first-order solution is a similarity solution, the generic mathematical challenge we focus on here is exploring how that similarity solution breaks down at second order. Significant spatio-temporal non-uniformities arise in the first-order similarity solution for the upper region, which are already complicated to handle: a snapshot of the front shape at a fixed very early time will have very sharp curvature, whereas a material point on the front released at a very early time will have rapid temporal changes in its vertical velocity component [27]. Hence, we have to

perturb the upper region about a solution that evolves over arbitrarily small spatial distances at arbitrarily small times: this then is where the challenge lies.

There is also a question concerning for which set of times a second-order solution might be valid given that in ref. [27], although the first-order solution was obtained formally for $t \ll 1$, it managed to describe the front shape reasonably well even for values of t up to order unity, as was determined by comparison with numerical results from an Eulerian model [32]. Hence, we expect the second-order solution should also be valid over a similar time domain. In ref. [32], the shape of a foam front in Eulerian coordinates was obtained numerically by solving a coupled system of Hamilton–Jacobi equations [33], where the foam front was given implicitly, as the zero-level set [34] of the solution variable. In the Eulerian method, it is not necessary to deal explicitly with the aforementioned incompatibility between the positioning of newly injected material points and material points already on the front, since material points are not tracked at all, by contrast with what is required in a Lagrangian method. Nonetheless, a concave corner or kink still arises. This kink was then tracked via an Eulerian scheme in ref. [32], and its position at early times was found to be consistent with the Lagrangian estimates from ref. [27]. Nevertheless, numerical artefacts may appear in the Eulerian solution since we can only ever capture the concave corner to within the numerical grid resolution. This then motivates a return to a Lagrangian approach to search for an improved analytical approximation, which will be free of such artefacts.

(c) Modelling the foam front

We can model the foam front advance through a homogeneous oil reservoir (figure 1) by using a dimensionless form of the ‘pressure-driven growth model’, which has been widely studied before [5,10,27,31,35]. The pressure-driven growth model relates the pressure difference across the propagating front to motion, which is in the local normal direction $\mathbf{n} = \hat{\mathbf{i}} \cos(\alpha) - \hat{\mathbf{j}} \sin(\alpha)$, oriented at an angle α below the horizontal (figure 1). For the purpose of Lagrangian computation, the propagation front can be discretized into a finite number of material points, the motion of which we can readily track, and the front shape itself at any given time can be reconstructed by following a collection of such points. The dimensionless form of the pressure-driven growth model, developed in refs. [5,10,27,36], and used in this work, establishes that at any local front position $\mathbf{x} = (x, y)$, the motion is governed by,

$$\frac{d\mathbf{x}}{dt} = \left(\frac{y}{s}\right) \mathbf{n}, \quad (1.1)$$

where $y \in [0, 1]$ represents the distance above the maximum depth (where $y = 0$ represents the bottom and $y = 1$ the top of the solution domain), s is the distance travelled by a material point and \mathbf{n} is the local normal direction. The boundary condition establishes that at the top ($y = 1$), front position x as a function of time corresponds to $\sqrt{2t}$ in a dimensionless form [37], and at this point, the front is completely perpendicular to the top (figure 1). A concave corner develops and shifts over time [27] (figure 1). This corner is also called a ‘matching point’ since it is where we must match two aforementioned regions that divide the front vertically: the ‘lower region’ incorporating material points originally on the front and the ‘upper region’ consisting of newly injected points. The upper region starts off being of arbitrarily small extent, but grows over time (the lower region shrinks to compensate). Likewise initially the front reorients by an arbitrarily small angle in the upper region (albeit with arbitrarily large curvature), but the amount it reorients grows over time (whereas curvature falls). Specifically, it was shown by [27] that the upper region is of vertical extent relative to the maximum penetration depth of the front of order t (t here being the dimensionless time), and it reorients through an angle of order \sqrt{t} , making curvature become order $1/\sqrt{t}$. As we have said, the concave corner arises as a consequence of an incompatibility between points originally on the front and newly injected points. So, the concave corner itself corresponds to the location on the front at which material points from either side meet. Both above and below the corner, it is possible to capture analytically for small times $t \ll 1$, how material points move. If we consider according to equation (1.1) that, closer to $y = 1$, the speed of the

points is faster, the sign of the \hat{j} component of the normal \mathbf{n} becomes negative (as in figure 1), which implies that the points are moving downwards, following

$$\frac{dy}{dt} = -\left(\frac{y}{s}\right) \sin(\alpha), \quad (1.2)$$

as well as moving in the x direction as

$$\frac{dx}{dt} = \left(\frac{y}{s}\right) \cos(\alpha), \quad (1.3)$$

with α being the angle by which \mathbf{n} is oriented below the horizontal. Combined together, equations (1.2) and (1.3) give us the evolution of the trajectory path length as follows:

$$\frac{ds}{dt} = \sqrt{\left(\frac{dx}{dt}\right)^2 + \left(\frac{dy}{dt}\right)^2} = \frac{y}{s}. \quad (1.4)$$

By approximating these equations, it is possible to track analytically for small times, the trajectory of the point that was originally at the top ($y = 1$ when $t = 0$). In particular for the vertical coordinate, this can be done at first order (order t) and also at second order (order t^2) (assuming this point has not been consumed by the concave corner) [10,27]. Horizontally, this point lags an order $t^{3/2}$ distance behind the top of the front (which is always at location $x = \sqrt{2t}$). The trajectory of this material point, which was initially at $y = 1$, gives an indication where the concave corner (or kink) may be, but not the exact location, since we are tracking a material point near the concave corner not the corner itself. As already mentioned, what was studied in refs. [10,27] is that the second-order correction causes the material point to move down more slowly than the first-order approximation predicts. Extending this analysis to material points initially at $y \leq 1$, a solution is obtained for the lower region [27], to be discussed in §2. In the upper region, front material points are tracked also, but this presents more of a challenge requiring, as mentioned earlier, a similarity solution to be developed (see §3).

To summarize, this work expands upon the methodology used in ref. [27] to obtain a second-order accurate solution to track the trajectory of the injected material points for $t \ll 1$, again, in terms of similarity variables in the upper region, but with small perturbations breaking the similarity. This proves challenging to do because of the strong spatio-temporal non-uniformities associated with the similarity solution. The perturbed solution will be used to find the intersection or matching point between the lower and the upper regions of the front (the concave corner or kink), consistently through to the second order. The solution will then be interrogated in an effort to establish which scenario (figure 2*a* or 2*b*) is realized as time progresses, noting that the scenario of figure 2*a* is necessarily realized at arbitrarily small times.

The rest of this work is laid out as follows. In §§2–4, we review the existing methodology derived by ref. [27], the extension to that methodology appearing from §5 onwards. The second-order solution will be expressed, as before, in terms of similarity variables, but admitting small perturbations at small times $t \ll 1$ that break the similarity (see §5). Then, in §§6 and 7, using this new solution we will proceed to track the position of the concave corner with an accuracy of second order in time t . Finally, in §8, we will use the second-order solution to compute the shape of the upper region of the front in comparison with the previous solution given in ref. [27]. Conclusions are offered in §9.

2. Front propagation in the lower region

This section reviews the theory for the lower region presented in ref. [27]. The key result we derive is equation (2.9), which describes the shape of the lower region. Readers familiar with the derivations from ref. [27] may want to skip directly to §3.

To determine the front lower region shape, we solve equations (1.2)–(1.4) for $t \ll 1$. For small times, the front is close to being a vertical line, the angle α being very small along it. So, we can estimate $\cos(\alpha) \approx 1$, via a leading order Taylor expansion. Moreover, we can also approximate the

trajectory as $s \approx x$. Hence, we can compute equation (1.3) as $dx/dt \approx y/x$. Then, after integration, we obtain that $x \approx \sqrt{2yt}$, which is known as the Velde solution [10,27]. A higher order solution known as the improved Velde solution was also given in ref. [27], establishing that

$$x \approx \sqrt{2yt + \frac{t^2}{6}}. \quad (2.1)$$

This solution recognizes that historically points have been higher up (and hence faster moving) than their current y location indicates. As a result, they have moved further than the Velde solution indicates, i.e. the x location computed by equation (2.1) is bigger than $x \approx \sqrt{2yt}$. Up until this point, we have the Velde solution of order $t^{1/2}$ and the improved Velde solution with a correction of order $t^{3/2}$, given the x displacement of the lower region of the front. We can also obtain an order t solution to compute the vertical location y of the points in the lower region (corresponding to a first-order solution). This solution can be derived for small times $t \ll 1$, starting from equation (1.2), with $s \approx \sqrt{2yt}$ and $\sin(\alpha) \approx \alpha \approx \tan(\alpha) \equiv dx/dy \approx \sqrt{t/(2y)}$, via the Velde solution. As long as α is small, the curvature of the front $d\alpha/dS$ (with S being measured down along the front as in figure 1) can then be approximated by $|d\alpha/dy| \approx t^{1/2}y^{-3/2}/(2\sqrt{2})$, so it is likewise a small quantity when $t \ll 1$. Using (2.1) in place of the Velde solution only perturbs this curvature slightly. This modest curvature in the lower region is a contrast from the order $1/\sqrt{t}$ curvature that turns out to be present in the upper region. Here, we have adopted the notation of [27], where d/dy denotes a derivative along a front composed of various material points at fixed t , whereas d/dt denotes a time derivative following a specified material point. Then, integrating equation (1.2), we determine

$$y \approx y_0 - \frac{t}{2}, \quad (2.2)$$

where y_0 is the initial position of a material point originally anywhere below the top $y_0 \leq 1$. Therefore, for the point initially at the top of the lower region ($y_0 = 1$), we can compute

$$y_{1st,lower} \approx 1 - t/2, \quad (2.3)$$

as its first-order approximated location over time. Considering that, at first order, all material points in the lower region migrate downwards with a vertical velocity component of $-1/2$, new material points must be injected to fill the gap between the $y_0 = 1$ point and the top of the reservoir. Hence, we can define a rescaled form for the vertical coordinate of the points as follows:

$$\zeta = \frac{(1-y)}{(t/2)}, \quad (2.4)$$

where ζ represents a ratio of distances between the top of the reservoir and any arbitrary point y on the front, divided by the vertical distance through which the material point initially at the top of the front has displaced. Here, at leading order, ζ takes values from $\zeta = 0$ at the top of the reservoir ($y = 1$), to $\zeta = 1$ for the topmost original material point of the lower region, with $\zeta > 1$ for points even lower down. However, a direct computation of the concave corner (or matching point between the lower and upper regions) found that it actually occurs at $\zeta = \zeta_{cross} < 1$ ($\zeta_{cross} \approx 0.954$, based on a complex integro-differential equation theory, changing to roughly $\zeta_{cross} \approx 0.94$ for a simpler but approximate differential equation approach), as shown in ref. [27]. The subscript ‘cross’ denotes the point at which upper and lower regions cross over one another, i.e. the corner or matching point we seek. Since the material points originally at the top of the front are now slightly lower down in y (slightly higher in ζ) than the kink or concave corner is, new material points have been extracted from the kink to fill the lower region (see e.g. figure 2a).

In addition, at any given y , we can define ξ as the horizontal displacement of the front, back from the leading edge at the top of the front $\sqrt{2t}$, given by

$$\xi = \sqrt{2t} - x. \quad (2.5)$$

We can also express ξ geometrically as follows:

$$\xi = \int_y^1 \left(\frac{dx}{dy} \right) dy = \int_y^1 \tan(\alpha) dy. \quad (2.6)$$

We cannot yet use equation (2.6) to determine ξ exactly, since it extends all the way into the upper region, for which α versus y is still unspecified. However, we can still use it to estimate the order of magnitude of ξ under the assumption that α (albeit not curvature approximated here by $|\alpha/dy|$) has a similar order of magnitude moving between the upper and lower regions. For small times $t \ll 1$, since $\alpha \approx \sqrt{t/(2y)}$ via the Velde solution (with $\alpha = \text{atan}(dx/dy) \approx dx/dy$), we define \mathcal{E} as, the rescaled in time horizontal displacement [27], follows:

$$\mathcal{E} = \xi/t^{3/2}, \quad (2.7)$$

which recognizes that ξ is an order $t^{3/2}$ quantity since we are integrating an order \sqrt{t} quantity over an order t distance in the y direction close to $y = 1$ (see equation (2.4)). Furthermore, we can express the lower region of the front, corresponding to $\zeta \geq \zeta_{\text{cross}}$, in terms of ζ and \mathcal{E} , by first substituting equation (2.1) into equation (2.5) to obtain

$$\xi = \frac{(2t - x^2)}{(\sqrt{2t} + x)} \approx \frac{(2t - 2yt - t^2/6)}{(\sqrt{2t} + x)}, \quad (2.8)$$

and then specifically near the top of the domain where $x \approx \sqrt{2t}$, we can obtain after introducing equations (2.4) and (2.7), that

$$\mathcal{E} \approx \frac{(\zeta - 1/6)}{(2\sqrt{2})}, \quad \text{if } \zeta \geq \zeta_{\text{cross}}, \quad (2.9)$$

where $\zeta \geq \zeta_{\text{cross}}$ here requires

$$y \leq y_{\text{cross}} \equiv 1 - \left(\frac{t}{2} \right) \zeta_{\text{cross}}, \quad (2.10)$$

which implies that (2.9) is a solution describing specifically the lower region up to the matching point or concave corner at location y_{cross} as defined by equation (2.10). The utility of equation (2.9) is that it gives a \mathcal{E} versus ζ relation for the lower region, and if we can also obtain a \mathcal{E} versus ζ relation for the upper region, we can find where the two regions intersect and hence determine ζ_{cross} . This is what ref. [27] achieved by expressing the upper region in terms of a similarity equation (see §3 and also, in the electronic supplementary material, §S1 along with §S2). Note that equation (2.9) is a leading order solution for \mathcal{E} , accurate to order $t^{3/2}$. Later on in §5, we introduce equation (5.4), which corresponds to an order $t^{5/2}$ accurate solution for the lower region, close to the concave corner, improving upon equations (2.1) and (2.9) (see also details in the electronic supplementary material, §S3).

Geometrically, equation (2.1) is a parabola, and equation (2.9) represents a tangent to that parabola at $y = 1 - t/2$ or equivalently at $\zeta = 1$, the geometrical distance between the parabola and its tangent being negligible at the current order of approximation. Having this approximation for the front lower region, it is possible to obtain a more accurate (second-order) estimate of the trajectory y as a function of time t for material points in the lower region, as an improvement over and above equation (2.2). As was proven in ref. [27], such points move obeying

$$y \approx y_0 - t/2 + 5t^2/(48y_0), \quad (2.11)$$

where $y_0 \leq 1$ is the initial location of the points when $t = 0$. Equation (2.11) is a perturbation of (2.2), indicating that when $t \ll 1$ all points move downwards with the same leading order velocity, and moreover, velocity changes away from this leading order value only gradually with time. So, assuming that the $y_0 = 1$ point (the point originally at the top of the front) has not been consumed yet by the concave corner, its location can still be tracked, and assuming it remains reasonably close to the concave corner itself (to the extent that the aforementioned value of $\zeta_{\text{cross}} \approx 0.94$ is relatively close to unity), we have an indication of where the junction between the upper and the

lower region might be using equation (2.11). Indeed, we can compute the approximate vertical location of the topmost original material point in the lower region as follows:

$$y_{2\text{nd},\text{lower}} \approx 1 - t/2 + 5t^2/48 \approx 1 - 0.5t + 0.1042t^2. \quad (2.12)$$

In summary, we have a first-order estimate of the kink location y_{cross} , given by equation (2.10), and a second-order estimate $y_{2\text{nd},\text{lower}}$ (equation (2.11)) for a material point that improves upon equation (2.3) and that we postulate is close to the kink location, although without a definitive proof. The reason that the estimate $y_{2\text{nd},\text{lower}}$ was so readily obtained is that the lower region is comparatively uniform in space and time when $t \ll 1$, i.e. low curvatures of the front and weak perturbations away from a leading order material point velocity. Our objective now is to obtain a second-order correction to the equation for y_{cross} . Before achieving that however we need to switch over focus to the upper region. As we will see, analysing the upper region proves to be challenging due to strong spatio-temporal non-uniformities that are present there.

3. First-order location of the upper region's material points

In this section, we review the methodology employed in ref. [27] to determine the first-order solution for the shape of the upper region of the front, in order to determine how it might match with the lower region. The key results we derive are equations (3.3)–(3.5), which describe the shape of the upper region of the front, parametrically, in terms of a parameter ψ , which represents the fraction of time that an injected point has been on the front. We start by introducing similarity equations in the upper region, and then based on these, we develop an order time t solution to compute the vertical y movement of the points of the front's upper region, along with an order $t^{3/2}$ expression for the x displacement. Readers familiar with the derivations from ref. [27] may prefer to skip directly to §4. Higher order corrections are considered later on in §5.

(a) Introducing similarity variables

As ref. [27] showed, if at any given small instant in time ($t \ll 1$), the location and orientation of a material element (treated as a set of closely spaced collinear material points) are identified relative to the overall extent of the upper region and overall amount that the upper region reorients (both of which happen to be arbitrarily small when $t \ll 1$), then it should be possible to collapse together the front shapes in the upper region at different instants of time into a self-similar form. Hence, we can express the front orientation angle α of the upper region as follows:

$$\alpha = \sqrt{\frac{t}{2}} A(\zeta), \quad (3.1)$$

where A is a function of the variable ζ defined earlier [27] (see also §S1 in the electronic supplementary material, which specifies the function implicitly as $\zeta = \zeta(A)$). If t is small here, α is likewise small. On the other hand, using (2.4) and (3.1), curvature $d\alpha/dS$, which is approximately $|d\alpha/dy|$, becomes $(t/2)^{-1/2} dA/d\zeta$ and hence is large when t is small. Note also that $\sqrt{t/2}$ is, at leading order, the amount that a material element reorients at the top of the lower region. This leading order estimate is obtained via the Velde solution since we are looking at small times $t \ll 1$ close to $y \approx 1$. Knowing the top of the lower region reorients to $\alpha \approx \sqrt{t/2}$, if we compare this with equation (3.1) for the upper region, any value of $A(\zeta)$ greater than unity at the bottom of the upper region thereby implies a concave kink. Moreover, the front meets the top perpendicularly, as the boundary condition at $y = 1$ requires that the angle $\alpha = 0$ there. This then implies that A varies from 0 at the top, to some value A_{cross} at the cross-over or matching point, estimated to be at $\zeta = \zeta_{\text{cross}}$. We know from ref. [27] that ζ_{cross} is slightly less than unity, so at leading order, the kink or concave corner moves down slightly more slowly than material points originally at the top of the lower region. Moreover ref. [27] showed that $A_{\text{cross}} \approx 1.18$ roughly, which is slightly greater than unity, so the upper region reorients more than the lower region does. As mentioned earlier, that is what produces the kink or corner.

(b) First-order upper region representation in terms of ψ

Since points originally on the front $y_0 \leq 1$ move downwards (as we demonstrated in §2), material points must be injected from the top onto the front [10] to have a continuous solution over time. For the upper region, we define t_{inj} as the time at which a material point has been injected. For a fixed time t , we require that $t_{\text{inj}} \in (0, t]$. As in ref. [27], we can define a coordinate ψ , such that $1 - \psi$ is the ratio between t_{inj} and t , as follows:

$$\psi = 1 - t_{\text{inj}}/t. \quad (3.2)$$

We can express the front location (coordinates ζ and \mathcal{E}) in terms of ψ instead of A (contrast §S1 in the electronic supplementary material). Here, ψ can be varied by fixing t and varying t_{inj} (thereby looking at a collection of different material points) or alternatively by fixing t_{inj} and varying t (following the trajectory of an individual material point): both ways of varying ψ turn out to be useful later on. If t_{inj} is significantly smaller than t , the points injected tend to be already close to the concave corner, implying that $\psi \rightarrow \psi_{\text{cross}}$. Here, $\psi_{\text{cross}} < 1$ (via the integro-differential theory, typically $\psi_{\text{cross}} \approx 0.948$ [27]; or alternatively $\psi_{\text{cross}} \approx 0.9431$ for the simpler differential equation approach to be employed here, see §7.4.3 in ref. [27]), corresponds to the maximum value of ψ , which is reached at the concave corner. Points with t_{inj} smaller than $(1 - \psi_{\text{cross}})t$ have already been consumed by the concave corner, so are no longer part of the propagating front (figure 2). By contrast, if $t_{\text{inj}} \rightarrow t$, the material points are near to the top, which implies that $\zeta \ll 1$, $A \ll 1$, $\mathcal{E} \ll 1$ and $\psi \ll 1$. To date, we have presented a first-order theory of the upper region as per ref. [27]. The second-order theory to be presented from §5 onwards is most naturally expressed in terms of the variable ψ defined by equation (3.2), rather than in terms of A as is presented in §S1 in the electronic supplementary material. Before tackling the second-order theory, therefore we need to recast the theory for the upper region in terms of ψ and then explain how to identify the matching point between the lower and upper regions.

As mentioned previously, at small times $t \ll 1$, we can collapse together the front shapes at different times, expressing the shape in terms of similarity variables A , ζ and \mathcal{E} , instead of α , y and ξ . In particular, assuming that the upper region of the front consists of a set of material points, each one injected at a different time $t_{\text{inj}} \in (0, t]$, we can compute the front shape for a fixed time t in terms of ψ , varying it between 0 up to some ψ_{cross} . It follows from ref. [27] that

$$A \approx A_0 \equiv \frac{(1 - (1 - \psi)^c)}{c}, \quad (3.3)$$

where $2c - 1$ is the assumed invariant ratio between ds/dy and dx/dy , over the upper region [27] (see §S1 in the electronic supplementary material). Substituting into equation (S1.2), we deduce

$$\zeta \approx \zeta_0 \equiv \frac{(1 - c\psi - (1 - \psi)^c)}{c(1 - c)}. \quad (3.4)$$

Equations (3.3)–(3.4) have been expressed in the form $A_0(\psi)$ and $\zeta_0(\psi)$ to highlight that they are leading order expressions that may need to be corrected as time increases. It can be readily checked that $d\zeta/dA \equiv (d\zeta/d\psi)/(dA/d\psi)$, when computed at leading order via equations (3.3)–(3.4), is compatible with equation (S1.1) (the original form given by [27]). We also obtain a leading order expression for the rescaled horizontal displacement of the upper region $\mathcal{E} = (2\sqrt{2})^{-1} \int_0^\zeta A d\zeta$ in the form $\mathcal{E} \approx \mathcal{E}_0(\psi)$, by substituting from equations (3.3)–(3.4) to give

$$\mathcal{E} \approx \mathcal{E}_0 \equiv \frac{2c((1 - \psi)^c - c - 1)\psi + (1 + c)(1 - \psi)^{2c} - 2(2c + 1)(1 - \psi)^c + 3c + 1}{4\sqrt{2}c^2(1 - c^2)}. \quad (3.5)$$

Taken together (3.4) and (3.5), both in terms of ψ , give a parametric representation of the upper region of the front, with the same order of accuracy in time as the lower region as computed by equation (2.9), i.e. order $t^{3/2}$ in ξ and order t in y . Therefore, we can determine in terms of ψ , the matching point between the lower and the upper region of the front. This is how ref. [27] proceeded to obtain ψ_{cross} , and the details will be discussed in the next section.

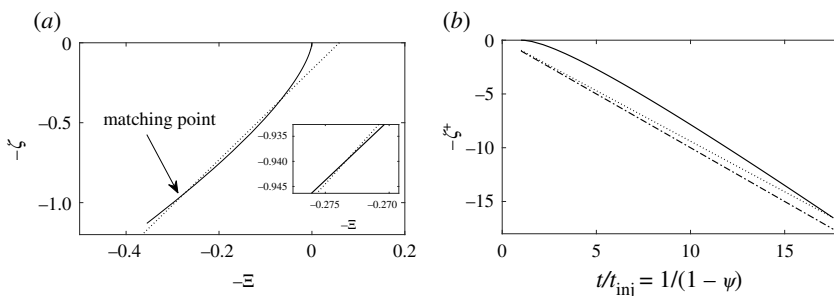


Figure 3. (a) Matching point between the lower (dotted line) and the upper (solid line) region of the front. Here, $-\zeta$ is the rescaled vertical y location of the front and $-\mathcal{E}$ is the rescaled horizontal displacement of the front behind the leading edge at the top. We decide to plot $-\mathcal{E}$ versus $-\zeta$ since it has the same orientation as x versus y . We obtain that the matching point occurs at $\psi_{\text{cross}} \approx 0.9431$. Here, $\zeta_{\text{cross}} \approx 0.9397$ and $\mathcal{E}_{\text{cross}} \approx 0.2733$. (b) Rescaled $-\zeta_+(\psi)$ location (see the electronic supplementary material, S52 for additional details) versus a rescaled time defined as $t/t_{\text{inj}} = 1/(1 - \psi)$ with $0 \leq \psi \leq \psi_{\text{cross}} \approx 0.9431$. The solid curve represents the trajectory $-\zeta_+(\psi)/(1 - \psi)$, with $\zeta(\psi) \equiv \zeta_0(\psi)$ at leading order as given by equation (3.4). Note this is not a straight line, implying non-uniform motion. The dotted line shows the $-\zeta_+$ position of the concave corner itself, namely, $-\zeta_{\text{cross}}/(1 - \psi)$, with $\zeta_{\text{cross}} \approx 0.9397$. The solid curve and the dotted line coincide only when $\psi = \psi_{\text{cross}} \approx 0.9431$. The dash-dotted line shows the trajectory in terms of $-\zeta_+$ of a point in the lower region that was originally at the top of the front, as $-1/(1 - \psi)$.

4. First-order matching point between upper and lower regions

Now we review the methodology used in ref. [27] to determine the first-order vertical location of the concave corner over time. Reviewing this enables us subsequently to extend that methodology to second order in S5. The key first-order results are shown in figure 3. A snapshot of the shape of the front is plotted in figure 3a, and in figure 3b, the trajectory of the concave corner at leading order is plotted, in comparison with the first-order approximated trajectory of material points in the upper and lower regions. Having consulted figures 3a–b, some readers may prefer to skip to S5, in which the methodology is extended to higher order solutions.

Our immediate objective via figure 3 is to obtain the first-order matching point between the lower and upper regions of the front (namely, the concave corner). We proceed by plotting both regions, using equation (2.9) for the lower region and equations (3.4)–(3.5) for the upper region, identifying the intersection or matching point (see figure 3a). Assuming $c = 3/4$ (the value given by [27], see the electronic supplementary material S51 for details), the matching point between these two regions turns out to be $\zeta_{\text{cross}} \approx 0.9397$ and $\mathcal{E}_{\text{cross}} \approx 0.2733$ and is obtained at $\psi_{\text{cross}} \approx 0.9431$ (figure 3a). This same result was previously obtained in ref. [27] albeit expressed not in terms of ψ but rather in terms of A (equations (S1.2)–(S1.3)), with the corner found at $A_{\text{cross}} \approx 1.18$ roughly. Given the value of ζ_{cross} , we can compute via equation (2.10)

$$y_{1\text{st,cross}} = 1 - 0.4698 t, \quad (4.1)$$

as the first-order vertical location of the concave corner (the cross-over or matching point between the upper and the lower region of the front). Here, we employ the notation $y_{1\text{st,cross}}$ (instead of simply y_{cross} used earlier) to emphasize that this is a first-order solution. In the rest of the section, we explore some consequences and concepts that follow from having found the first-order matching point. These will be generalized to second order in later sections of the paper.

Further details can be found in the electronic supplementary material, S52, which based on the value of ψ_{cross} defines $t_{\text{inj}(\text{min})}(t)$ (the earliest injected point still surviving on the front at time t) and $t_{\text{max}}(t_{\text{inj}})$ (the maximum time out to which a point injected at t_{inj} survives). Electronic supplementary material S52, also presents another rescaling of the y coordinate $\zeta_+ = (1 - y)/(t_{\text{inj}}/2) = \zeta/(1 - \psi)$, which is relevant to figure 3b. While the variable ζ is useful for

representing the shape of the front at fixed t , the variable ζ_+ is more useful for representing the trajectory of a material point with fixed t_{inj} . Indeed, for a fixed t_{inj} (and hence fixed material point), plotting ζ_+ versus $1/(1 - \psi)$ (with $1/(1 - \psi) = t/t_{\text{inj}}$ via equation (3.2)) is just a rescaling of y versus t . The fact that this is not a straight line in figure 3*b* indicates that, in the upper region, material point motion always varies with time even in the limit of very small t_{inj} and hence very small t : this is one of the challenges of tracking material points in the upper region.

5. Second-order correction to front shape

To date, all we have done is review the first-order findings of [27], recast in terms of a more convenient variable set. Now we extend those findings to obtain a second-order accurate solution in time to compute the upper and lower regions of the front. Key results we obtain are equations (5.5)–(5.7), from which we can track upper region material points on the front, and equation (5.8), for which we can compute the corresponding location of points in the lower region. Some details are relegated to the electronic supplementary material §§S3 and S4.

(a) Second-order location of the upper region's material points

Although we parameterize the system in terms of ψ here, if we recall that ζ and Ξ could also be expressed readily in terms of A (see equations (S1.2) and (S1.3), respectively), it is useful to begin by computing a second-order expression for the front orientation angle A , for a small but finite time t (see the electronic supplementary material §S4a for details of how this is achieved). It is reasonable to expand A as follows:

$$A(\psi, t) \approx A_0(\psi) + t A_1(\psi), \quad (5.1)$$

to determine the effect of an order t correction upon the rescaled front orientation angle A (which corresponds to an order $t^{3/2}$ correction for α , see equation (3.1)). Equation (5.1) breaks the similarity solution depending as it does on both ψ and t , not merely on ψ . Consistently, we can expand the rescaled vertical (see the electronic supplementary material §S4b for details) and horizontal (see the electronic supplementary material §S4c for details) locations of the upper region's material points, respectively, in the form of

$$\zeta(\psi, t) \approx \zeta_0(\psi) + t \zeta_1(\psi) \quad (5.2)$$

and

$$\Xi(\psi, t) \approx \Xi_0(\psi) + t \Xi_1(\psi). \quad (5.3)$$

Here, A_0 , ζ_0 and Ξ_0 from §3, and A_1 , ζ_1 and Ξ_1 computed in the electronic supplementary material §S5, turn out to be well-defined quantities in terms of ψ . In addition, since ζ is related to y via equation (2.4) and Ξ is related to ξ via equation (2.7), and hence to x via equation (2.5), it follows that equations (5.2) and (5.3) are order t^2 and $t^{5/2}$ accurate expressions in y and x , respectively. To use these expressions to find the matching point between both regions of the front, we must also calculate, with a consistent order of accuracy, the shape of the lower region.

(b) Second-order correction to lower region front shape

We now present an extension of the equation (2.9), used to compute the lower region of the front. Note that the equation (2.9) has been derived via an order $t^{3/2}$ accurate solution in the x direction (given by equation (2.1); also known as the improved Velde solution) and an order t accurate solution in the y direction (given by equation (2.2)). We need, however, to incorporate the order t^2 effect, in the vertical, which is given by equation (2.11), along with an order $t^{5/2}$ correction to compute the x location of material points, to achieve the same order of accuracy as is computed

for the upper region via equations (5.2) and (5.3). The required expression is (see the electronic supplementary material §S3)

$$\mathcal{E} \approx \frac{1}{2\sqrt{2}} \left(\zeta - \frac{1}{6} + \frac{t}{8} \left(\zeta^2 - \frac{\zeta}{3} + \frac{107}{540} \right) \right), \quad \text{if } \zeta \geq \zeta_{\text{cross}}, \quad (5.4)$$

which represents a parabola, as it includes a second-order term in ζ . This is applicable specifically near the top of the lower region ($\zeta \geq \zeta_{\text{cross}}$ but not $\zeta \gg 1$). Here, we see how a self-similar solution (given by equation (2.9) involving only \mathcal{E} and ζ), valid for early times, is broken at a small but finite time. According to equation (5.4), for any specified ζ , the order t correction term for \mathcal{E} is positive, so on a graph such as figure 3a, which plots coordinates $(-\zeta, -\mathcal{E})$, we obtain a point to the left of the $t \rightarrow 0$ limit (dotted line in figure 3a).

(c) Rescaled location of the upper region's material points

The form of equations (5.1), (5.2), (5.3) (upper region) and (5.4) (lower region) indicates that in the limit $t \rightarrow 0$, the upper region can be expressed in similarity form via variables ζ and \mathcal{E} , in which for the upper region in particular, only the ratio $t_{\text{inj}}/t \equiv 1 - \psi$ was relevant. Nevertheless, for small but finite t , the similarity solution is broken as alluded to earlier, and both values t_{inj} and t are needed. To explore how the similarity solution becomes broken, we can either select a given t and find the front shape ζ versus \mathcal{E} at that time, or alternatively we can select a given t_{inj} and find how a material point injected at time t_{inj} moves and reorients. This latter approach is easier since the governing equations for pressure-driven growth are expressed in the Lagrangian form. A rescaling of the variables is now convenient. We define ζ_+ and \mathcal{E}_+ , as the rescaled $1 - y$ and $\sqrt{2}t - x$ front location, rescaling respectively, by amounts depending solely on the now fixed t_{inj} (respectively by $t_{\text{inj}}/2$ and $t_{\text{inj}}^{3/2}$), and we track a material point trajectory parametrically by varying ψ from 0 up to ψ_{cross} (the matching point between the lower and upper region). Consistently, we define A_+ as the rescaled front orientation angle α (rescaled by $\sqrt{t_{\text{inj}}/2}$). Using definitions analogous to equations (2.4), (2.7) and (3.1), but with t_{inj} in place of t , and relating A_+ , ζ_+ and \mathcal{E}_+ back to A , ζ and \mathcal{E} , we compute via equations (5.1)–(5.3)

$$A_+ \approx \frac{A_0(\psi)}{\sqrt{1-\psi}} + t \frac{A_1(\psi)}{\sqrt{1-\psi}} \equiv A_{+,0}(\psi) + t_{\text{inj}} \frac{A_1(\psi)}{(1-\psi)^{3/2}} = A_{+,0}(\psi) + t_{\text{inj}} A_{+,1}(\psi), \quad (5.5)$$

$$\zeta_+ \approx \frac{\zeta_0(\psi)}{1-\psi} + t \frac{\zeta_1(\psi)}{1-\psi} \equiv \zeta_{+,0}(\psi) + t_{\text{inj}} \frac{\zeta_1(\psi)}{(1-\psi)^2} = \zeta_{+,0}(\psi) + t_{\text{inj}} \zeta_{+,1}(\psi), \quad (5.6)$$

$$\text{and } \mathcal{E}_+ \approx \frac{\mathcal{E}_0(\psi)}{(1-\psi)^{3/2}} + t \frac{\mathcal{E}_1(\psi)}{(1-\psi)^{3/2}} \equiv \mathcal{E}_{+,0}(\psi) + t_{\text{inj}} \frac{\mathcal{E}_1(\psi)}{(1-\psi)^{5/2}} = \mathcal{E}_{+,0}(\psi) + t_{\text{inj}} \mathcal{E}_{+,1}(\psi), \quad (5.7)$$

where t has been replaced by $t_{\text{inj}}/(1-\psi)$ (as follows from equation (3.2)). Hence, if we can determine how the front shape is perturbed at any given $t \ll 1$ (given by equations (5.1)–(5.3)), we can also determine how the trajectory of a material point is perturbed at any given t_{inj} , i.e. for different choices of $t_{\text{inj}} \ll 1$, we have different solutions of \mathcal{E}_+ and ζ_+ versus ψ , which correspond to the actual geometric path that a fixed injected material point takes (at least to second-order accuracy) to reach the concave corner (the intersection with the lower region).

(d) Rescaled location of the lower region's material points

To find where material points injected in the upper region from time t_{inj} intersect the lower region, we convert (5.4) (applicable near the top of the lower region) into $\mathcal{E}_+ \equiv \mathcal{E}/(1-\psi)^{3/2}$ versus $\zeta_+ \equiv \zeta/(1-\psi)$ format. At any given time $t = t_{\text{inj}}/(1-\psi)$, it follows via equation (5.4)

$$\mathcal{E}_+ \approx \frac{(1-\psi)^{-3/2}}{2\sqrt{2}} \left(\zeta_+(1-\psi) - \frac{1}{6} + \frac{t_{\text{inj}}}{8} \left(\zeta_+^2(1-\psi) - \frac{\zeta_+}{3} + \frac{107}{540(1-\psi)} \right) \right), \quad (5.8)$$

where given any t_{inj} , our challenge is to find a ψ value (and hence a time t) at which equations (5.6) and (5.7) intersect equation (5.8). Therefore, equations (5.6) and (5.7) give a locus ζ_+ and \mathcal{E}_+

swept out by a material point in the upper region, and equation (5.8) gives the \mathcal{E}_+ that would be in the lower region at that same ζ_+ . The upper and lower regions only meet when, at the same ζ_+ , they also have the same \mathcal{E}_+ . This then gives the matching or cross-over $\zeta_{+\text{cross}}$ and $\mathcal{E}_{+\text{cross}}$ point: for additional details, see §S6 in the electronic supplementary material. Despite the similarity between equations (5.4) and (5.8), note the subtle difference in the way we use them. With equation (5.4), it is convenient to fix t and consider how \mathcal{E} varies with ζ at that fixed t . With equation (5.8), however, we vary t (by varying ψ at given t_{inj}) and select a particular ζ_+ (depending on ψ and hence on t), considering how \mathcal{E}_+ then varies. Therefore, tracking different t_{inj} gives different cross-over points $\zeta_{+\text{cross}}$ and $\mathcal{E}_{+\text{cross}}$, which can be expressed in a form giving the ζ_{cross} and $\mathcal{E}_{\text{cross}}$ location of the concave corner over time t : see §6 and also the electronic supplementary material §S7 for details. After using equation (5.8) in the way described earlier to locate the matching point, there turns out to be an alternative way in which this equation can be used. Given the ψ and ζ_+ values at the matching point, respectively ψ_{cross} and $\zeta_{+\text{cross}}$, it is possible to find, for any given t_{inj} , corresponding values of t and y at the matching point. For these specific t and y values, equation (2.11) can then be used to identify a y_0 value (i.e. a material point in the lower region, labelled by its initial location on the front), which coincides at the concave corner with the given upper region material point labelled by t_{inj} . It turns out (see §S8 in the electronic supplementary material) that the required y_0 only differs from unity by order t_{inj} amounts, so it is more useful to define a quantity $z_0 = 1 - y_0$ and hence a quantity Z_0

$$Z_0 \equiv \frac{(1 - y_0)}{(t_{\text{inj}}/2)} = \frac{z_0}{(t_{\text{inj}}/2)}. \quad (5.9)$$

Once y_0 or equivalently Z_0 is known for any given t_{inj} , then at all times t up the matching point, equation (2.11) can now be rescaled into ζ_+ versus ψ coordinates (see §S8 in the electronic supplementary material for details), giving the trajectory followed by the lower region material point, generally having (at any given time t or equivalently at any given ψ) a ζ_+ different from the upper region material point (except at the matching point). Substituting the lower region ζ_+ into equation (5.8) and varying ψ gives the trajectory followed over time by this material point in terms of ζ_+ versus \mathcal{E}_+ , which can be compared with the trajectory for the upper region material point described by equations (5.6)–(5.7). Trajectories of both points can be followed over time, and at the matching point they coincide. Before equation (5.8) can be used in this particular fashion however, first the matching point itself must be found.

6. Perturbed location of the concave corner

In this section, we present the perturbation analysis to track the location of the concave corner with second-order accuracy in time. The key result is equation (6.7), giving the vertical location of the concave corner over time. This is what we contrast, in §7, with the first-order solution for the corner given by equation (4.1). The analysis proceeds as follows. Given a set of small but finite t_{inj} values here, we can obtain different ψ_{cross} values, with which we can determine the variation in location of the concave corner over time. In the limit when $t_{\text{inj}} \rightarrow 0$, the value we seek is the aforementioned $\psi_{\text{cross}} \approx 0.9431$ (which we now denote $\psi_{\text{cross},0}$). More generally, however, varying t_{inj} will cause ψ_{cross} (obtained as per the procedure discussed in §5d) to vary also. In the limit of sufficiently small t_{inj} , we can approximate this variation via

$$\psi_{\text{cross}} \approx \psi_{\text{cross},0} + t_{\text{inj}}\psi_{\text{cross},1} \approx \psi_{\text{cross},0} + (1 - \psi_{\text{cross},0})\psi_{\text{cross},1}t. \quad (6.1)$$

Here, as mentioned earlier, $\psi_{\text{cross},0}$ is the lowest order approximation found previously, and $\psi_{\text{cross},1}$ is a next order correction to be determined. Knowing ψ_{cross} , we can also define additional quantities t_{max} and $t_{\text{inj}(\text{min})}$ (mentioned in §4 and defined in the electronic supplementary material §S2). Substituting (6.1) into equation (S2.2) and Taylor expanding, we deduce that the maximum

time $t = t_{\max}$ for which a material point injected at t_{inj} could survive would be

$$t_{\max} \equiv \frac{t_{\text{inj}}}{(1 - \psi_{\text{cross}})} \approx \frac{t_{\text{inj}}}{1 - \psi_{\text{cross},0}} + \frac{t_{\text{inj}}^2 \psi_{\text{cross},1}}{(1 - \psi_{\text{cross},0})^2}. \quad (6.2)$$

Moreover, at the cross-over point, the earliest injected material point still surviving at time t has $t_{\text{inj}} = t_{\text{inj}(\min)}$ with, according to equations (6.1) and (S2.1)

$$t_{\text{inj}(\min)} \equiv (1 - \psi_{\text{cross}})t \approx (1 - \psi_{\text{cross},0})t - (1 - \psi_{\text{cross},0})\psi_{\text{cross},1}t^2. \quad (6.3)$$

Although the discussion of §§5c–d focused on functions used for tracking the loci of material points, i.e. fixed t_{inj} , having the value of $t_{\text{inj}(\min)}$ can also be useful. Knowing $t_{\text{inj}(\min)}$ makes it possible to reconstruct the shape of the upper region (fixed t) by selecting a set of injected points t_{inj} in the domain $t_{\text{inj}(\min)} \leq t_{\text{inj}} \leq t$. Then, computing $\psi = 1 - t_{\text{inj}}/t$ for each one and computing \mathcal{E} and ζ (given by equations (5.3) and (5.2), respectively) for each ψ at the given time t , we can reconstruct the front shape. Thus, we can convert between material point trajectories and front shapes. This will be explored further in §8.

Once we know the values of $\psi_{\text{cross},0}$ and $\psi_{\text{cross},1}$, we can determine the perturbed value of A_+ at the concave corner (denoted $A_{+\text{cross}}$) by using equation (5.5) as follows:

$$A_{+\text{cross}} \approx A_{+,0}(\psi_{\text{cross},0} + t_{\text{inj}}\psi_{\text{cross},1}) + t_{\text{inj}}A_{+,1}(\psi_{\text{cross},0} + t_{\text{inj}}\psi_{\text{cross},1}), \quad (6.4)$$

which upon expanding for sufficiently small t_{inj} gives

$$\begin{aligned} A_{+\text{cross}} &\approx A_{+,0}(\psi_{\text{cross},0}) + t_{\text{inj}} \left(\psi_{\text{cross},1}A'_{+,0}(\psi_{\text{cross},0}) + A_{+,1}(\psi_{\text{cross},0}) \right) \\ &\equiv A_{+\text{cross},0} + t_{\text{inj}}A_{+\text{cross},1}, \end{aligned} \quad (6.5)$$

where $A'_{+,0}$ denotes the function $dA_{+,0}/d\psi$ (which is obtained via equations (3.3) and (5.5)). There are analogous expressions for ζ_+ and \mathcal{E}_+ at the concave corner (denoted $\zeta_{+\text{cross}}$ and $\mathcal{E}_{+\text{cross}}$): the formulae are given in equations (S7.1)–(S7.3) in the electronic supplementary material §S7. There are also analogous expressions, but expanded in terms of t rather than in terms of t_{inj} . These provide the cross-over values of A , ζ and \mathcal{E} , denoted A_{cross} , ζ_{cross} and $\mathcal{E}_{\text{cross}}$: see equations (S7.5)–(S7.7) in the electronic supplementary material.

Various ways to estimate the location of the concave corner in an effort to improve upon the first-order estimate $y_{1\text{st,cross}}$ already given in equation (4.1), now present themselves. Based on the definition of $\zeta_+ \equiv (1 - y)/(t_{\text{inj}}/2)$, we can obtain by tracking the vertical location of a given injected material point t_{inj} over time up to its intersection with the concave corner, an estimate of the y location of the corner. We denote this by $y_{\text{cross}}^{\text{inter}}$, i.e. the value of the matching point determined by this intersection, and it turns out to be

$$y_{\text{cross}}^{\text{inter}} = 1 - (t_{\text{inj}}/2) \zeta_{+\text{cross}}(t_{\text{inj}}). \quad (6.6)$$

Here, $\zeta_{+\text{cross}}(t_{\text{inj}})$ is obtained as already mentioned by tracking t_{inj} on the upper region using equations (5.6)–(5.7), until its location coincides with the lower region given by equation (5.8). The value of $\zeta_{+\text{cross}}(t_{\text{inj}})$ determined here will not agree perfectly with the expression obtained via a small t_{inj} expansion for $\zeta_{+\text{cross}}$ (see equation (S7.2) in the electronic supplementary material), although agreement should be good when t_{inj} is sufficiently small. We can combine this expression for $y_{\text{cross}}^{\text{inter}}$ versus t_{inj} with an expression for time at cross-over $t = t_{\text{inj}}/(1 - \psi_{\text{cross}})$ versus t_{inj} , this latter expression again not agreeing perfectly with the Taylor-expanded form given in (6.2). Despite these small discrepancies, a parametric representation of the cross-over y versus time t can now be obtained by varying t_{inj} . A slightly different estimate for the second-order vertical location of the concave corner over time t can be obtained by combining equation (2.10)

Table 1. Parameters for equations (6.1), (S7.1)–(S7.3), (S7.5)–(S7.7) (given in the S57 in the electronic supplementary material) and (6.7).

$\psi_{\text{cross},0}$	$\psi_{\text{cross},1}$	$A_{+\text{cross},0}$	$A_{+\text{cross},1}$	$\zeta_{+\text{cross},0}$	$\zeta_{+\text{cross},1}$	$\mathcal{E}_{+\text{cross},0}$	$\mathcal{E}_{+\text{cross},1}$
0.9431	0.4608	4.94	16.11	16.52	81.64	20.15	211.28
		$A_{\text{cross},0}$	$A_{\text{cross},1}$	$\zeta_{\text{cross},0}$	$\zeta_{\text{cross},1}$	$\mathcal{E}_{\text{cross},0}$	$\mathcal{E}_{\text{cross},1}$
		1.1784	−0.0528	0.9397	−0.1686	0.2733	−0.0257

with a small t expansion for ζ_{cross} in equation (S7.6), obtaining

$$y_{2\text{nd,cross}} \approx 1 - \left(\frac{t}{2}\right) \zeta_{\text{cross},0} - \left(\frac{t^2}{2}\right) \zeta_{\text{cross},1}. \quad (6.7)$$

In the limit of sufficiently small t , this should agree with what (6.6) predicts, but is rather simpler to evaluate. Provided we can determine $\zeta_{\text{cross},1}$ (the value of $\zeta_{\text{cross},0}$ being already known from the literature [27]; see also table 1), we can estimate the second-order position of the concave corner over time. Predictions for how second-order effects perturb not only the concave corner but also material point trajectories are discussed in the next section.

7. Second-order matching between upper and lower regions

In this section, we determine the effect of selecting a small but finite time upon the evolution of the upper region of the front, and how the matching point between the lower and the upper region moves with time. Recall that we are working with second-order accuracy in time, in the sense that we have included an order t^2 correction (newly derived here for the upper region, but already given by [27] in the case of the lower region) to compute vertical location y , and an order $t^{5/2}$ expression in time (newly derived in the present work) to compute the horizontal position x or ξ of a material point, with a consistent order of accuracy in time for both upper and lower regions. After suitable rescaling, this is given by equations (5.2) and (5.3) for the upper region, and equation (5.4) for the lower region. To measure the concave corner location over time, we use equations (5.7) and (5.6) to compute the (\mathcal{E}_+, ζ_+) location of the upper region's material points, which is done by fixing t_{inj} (following the trajectory of a specific material point) and then tracking (parametrically in terms of ψ) the locus swept out by the material point, up to the matching point with the lower region, with a (\mathcal{E}_+, ζ_+) location given by equation (5.8). To find the intersection where the two regions meet (see the discussion in §5d), it is sufficient to focus on a point in the lower region with the same ζ_+ value as the material point in the upper region, and determine the corresponding \mathcal{E}_+ value via (5.8). This is what is plotted in figure S2 in §S6 in the electronic supplementary material. When the location of the matching point is found, however, we can identify which specific material point from the lower region (identified by the value of Z_0 via equation (5.9)) happens to be present there (again see the discussion in §5d and details in §8). Then trajectories of both upper and lower region material points can be tracked until their intersection. This is what is plotted here in figure 4. In figure 4, we see that the matching point is slightly sensitive to t_{inj} . Increasing t_{inj} causes it to shift to the left (i.e. larger \mathcal{E}_+) and also slightly downwards (larger ζ_+). We also note from figure 4 that values of Z_0 are negative (see more explanation in the electronic supplementary material §S8). This implies y_0 values in excess of unity, i.e. points not actually present on the front initially, but which instead are extracted from the corner into the lower region as the system evolves. Although figure 4 only shows two t_{inj} values ($t_{\text{inj}} \rightarrow 0$ and $t_{\text{inj}} = 0.01$), we have repeated the calculations for a number of t_{inj} values in the domain $t_{\text{inj}} \in [0, 0.01]$, determining in each case the ψ value, namely ψ_{cross} , at which these points meet the concave corner (figure 5) and hence the maximum survival time $t_{\text{max}}(t_{\text{inj}})$, which is also estimated at least for $t_{\text{inj}} \ll 1$ by equation (6.2) (figure 6). We can also compute A_+ , ζ_+ , and \mathcal{E}_+ at the concave corner (figure 7a–c), and then

(by employing equations (5.5)–(5.7)), A , ζ and \mathcal{E} values there (figure 7d–f). These expressions plotted in figure 7 break similarity by allowing separate dependence on t_{inj} and t , rather than holding all values fixed at the matching point. At sufficiently small t_{inj} and/or t , we expect variation in all the aforementioned quantities to be linear in t_{inj} and/or t , as established by equations (S7.1)–(S7.3) and (S7.5)–(S7.7), respectively (as given in the electronic supplementary material S7). Here, we achieve this by focusing first on exceedingly small times $t_{inj} \in [0, 0.0001]$, thereby obtaining parameters for equations (6.1), (S7.1)–(S7.3), (S7.5)–(S7.7) and subsequently for (6.7), i.e. we obtain first $\psi_{cross,0}$ and $\psi_{cross,1}$ using data for $t_{inj} \in [0, 0.0001]$, from which we compute $A_{+cross,0}$, $A_{+cross,1}$, $\zeta_{+cross,0}$, $\zeta_{+cross,1}$, $\mathcal{E}_{+cross,0}$ and $\mathcal{E}_{+cross,1}$, and subsequently $A_{cross,0}$, $A_{cross,1}$, $\zeta_{cross,0}$, $\zeta_{cross,1}$, $\mathcal{E}_{cross,0}$ and $\mathcal{E}_{cross,1}$. These values are summarized in table 1. Note that although $A_{cross,0}$, $\zeta_{cross,0}$ and $\mathcal{E}_{cross,0}$ can be straightforwardly expressed in terms of $A_{+cross,0}$, $\zeta_{+cross,0}$ and $\mathcal{E}_{+cross,0}$ and $\psi_{cross,0}$ (see equations (5.5)–(5.7)), the relations for $A_{cross,1}$, $\zeta_{cross,1}$ and $\mathcal{E}_{cross,1}$ in equations (S7.5)–(S7.7) are rather more complex, and these quantities can even have opposite sign from $A_{+cross,1}$, $\zeta_{+cross,1}$ and $\mathcal{E}_{+cross,1}$ in equations (S7.1)–(S7.3), as in fact is obtained here (table 1). How such sign changes can arise is discussed in the electronic supplementary material S7. The aforementioned sign changes have the following implication. In a view such as figure 4, $-\mathcal{E}_+$ versus $-\zeta_+$, which compares trajectories of material points released at different t_{inj} , we have already seen that increasing t_{inj} drives the concave corner to the left and downwards, with the leftward shift being particularly noticeable due to the large $\mathcal{E}_{+cross,1}$ value in table 1. On the other hand, since $\zeta_{cross,1}$ and $\mathcal{E}_{cross,1}$ are negative, snapshots of the instantaneous front shape at various times t , using now $-\zeta$ versus $-\mathcal{E}$ coordinates in a view similar to Figure 3a, would show the corner shifting upwards and to the right, the upward shift being dominant owing to $\mathcal{E}_{cross,1}$ in table 1 being very small. In addition, the negative value of $A_{cross,1}$ implies that the jump in angle at the concave corner is less than first-order theory predicts, but since $A_{cross,1}$, like $\mathcal{E}_{cross,1}$, is numerically small in table 1, the shift in jump angle is likewise small compared with the vertical shift of the corner. The fact that fixing t produces a vertical shift in the corner location, whereas fixing t_{inj} produces a horizontal shift, indicates how the similarity solution breaks down, i.e. the solution no longer depends solely on the ratio t_{inj}/t . We now return to consider t_{inj} values in the domain, $t_{inj} \in [0, 0.01]$, instead of the much narrower domain $t_{inj} \in [0, 0.0001]$ used to obtain the data of table 1. In figure 5, we see ψ_{cross} as a function of t_{inj} , and it is clear that only for small times ($t_{inj} \leq 0.002$), we can consider the relation for ψ_{cross} to be a linear function well approximated by $\psi_{cross} \approx \psi_{cross,0} + t_{inj}\psi_{cross,1}$ (given by equation (6.1)), with values of $\psi_{cross,0}$ and $\psi_{cross,1}$ given by table 1. Nonetheless, at least in the domain of figure 5, we found that as t_{inj} increases, the matching point ψ_{cross} still manages to increase albeit deviating from equation (6.1). The values of ψ_{cross} now affect the behaviour of a number of other quantities (t_{max} , $t_{inj(min)}$) as well as A_{+cross} , ζ_{+cross} , \mathcal{E}_{+cross} , A_{cross} , ζ_{cross} and \mathcal{E}_{cross}) as we explain below, with an impact in turn on the corner's vertical y coordinate location (as we go on to explain).

(a) Values of t_{max} versus t_{inj} and $t_{inj(min)}$ versus t

As has been indicated already in §§4 and 6, for a given fixed t_{inj} , we can calculate the maximum survival times $t_{max}(t_{inj})$ (time at which the injected point t_{inj} reaches the concave corner). This is obtained by equations (S2.2) (as given in the electronic supplementary material) and/or via an expansion (6.2) and is what figure 6a shows. Equivalently (see figure 6b) for a given t we can determine the injection time $t_{inj(min)}$ of the earliest injected point still surviving (see equation (6.3)). From the data in figure 5 and table 1, specifically via the linear approximation of ψ_{cross} in (6.1), we evaluate equations (6.2) and (6.3), as

$$\frac{t_{max}}{t_{inj}} \approx 17.57 + 142.33 t_{inj} \quad (7.1)$$

and

$$\frac{t_{inj(min)}}{t} \approx 0.0569 - 0.0262 t, \quad (7.2)$$

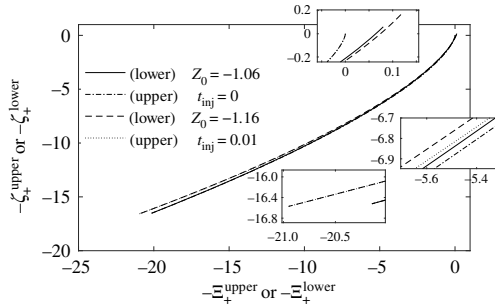


Figure 4. Trajectory of fixed material points labelled by t_{inj} in the upper region and fixed material points labelled by $Z_0 \equiv (1 - \gamma_0)/(t_{inj}/2)$ in the lower region in terms of rescaled vertical and horizontal distances ζ_+ and \mathcal{E}_+ . Dash-dotted line for upper region $t_{inj} = 0$ versus solid line for lower region $Z_0 \approx -1.06$ (see §S8 in the electronic supplementary material for an explanation of how to determine this Z_0 value). Dotted line for $t_{inj} = 0.01$ versus dashed line for $Z_0 \approx -1.16$. The curves are close to overlapping along almost all the trajectory, although they only intersect at the matching point $(\mathcal{E}_{+cross}, \zeta_{+cross})$.

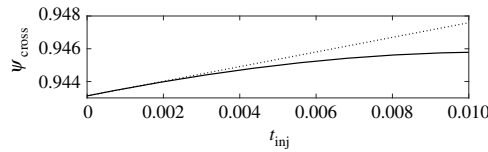


Figure 5. ψ_{cross} as a function of t_{inj} . Solid line: value ψ_{cross} of the matching point tracked up to time $t_{inj} = 0.01$. Dotted line: linear approximation obtained from data up to time $t_{inj} = 0.0001$, with $\psi_{cross} \approx \psi_{cross,0} + t_{inj}\psi_{cross,1}$ and for $\psi_{cross,0} \approx 0.9431$ and $\psi_{cross,1} \approx 0.4608$.

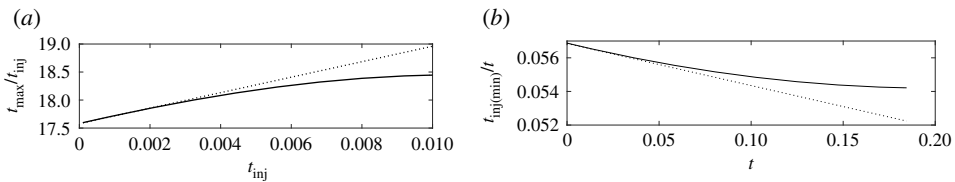


Figure 6. (a) Maximum survival time, for a given injected material point. Solid line: t_{max}/t_{inj} versus t_{inj} , given by equation (S2.2) (as given in the electronic supplementary material). Dotted line: approximation given by equation (7.1). (b) Minimum injection time of all surviving material points as a function of time. Solid line: $t_{inj(min)}/t$ versus t , given by equation (S2.1). Dotted line: approximation given by equation (7.2).

which are also plotted in figures 6*a,b*, respectively. Overall, equations (7.1) and (7.2) represent, at least for small time, good approximations to the values of t_{max} and $t_{inj(min)}$. Note in particular that $t_{inj(min)}/t \equiv 1 - \psi_{cross}$ (see equation (S2.1) in the electronic supplementary material), so the data in figure 6*b* mirror those in figure 5.

(b) Values of A_{+cross} , ζ_{+cross} , \mathcal{E}_{+cross} , A_{cross} , ζ_{cross} and \mathcal{E}_{cross}

Using ψ_{cross} obtained from figure 5, we can also determine evolution of the orientation and position of the concave corner over time, by evaluating either equations (5.5)–(5.7) or equations (5.1)–(5.3) setting also $t = t_{max}(t_{inj})$ via figure 6*a*. The behaviour is as follows (figure 7). In figures 7*a–c*, we see how A_{+cross} , ζ_{+cross} and \mathcal{E}_{+cross} (i.e. values at the concave corner), respectively, increase at early times as t_{inj} increases, and then, at slightly larger t_{inj} , are predicted

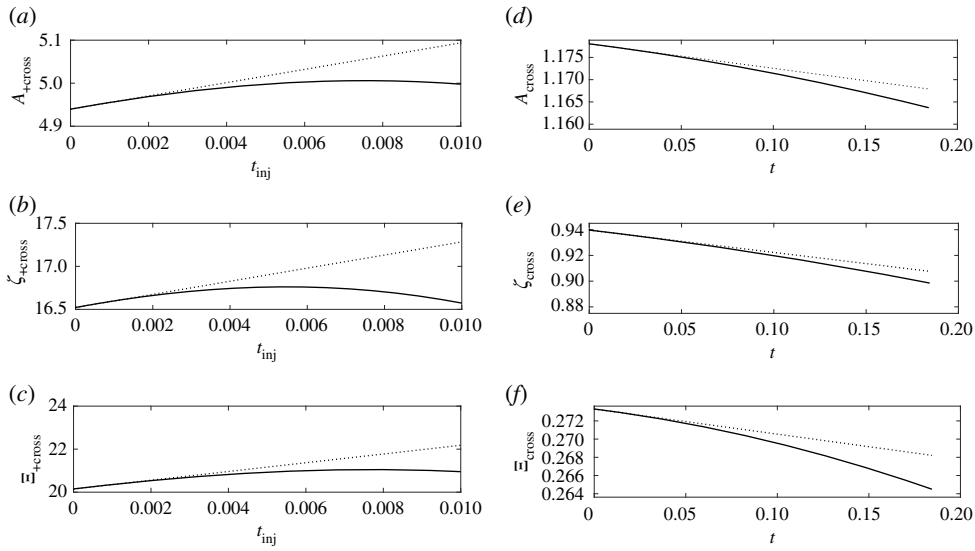


Figure 7. Values of variables at the matching point over time t_{inj} or t . Different computations of (a) A_{+cross} , (b) ζ_{+cross} and (c) Ξ_{+cross} for $t_{inj} \leq 0.01$. These are obtained, respectively, by equations (5.5)–(5.7) evaluated at ψ_{cross} (solid lines), and by equations (S7.1)–(S7.3) (dotted lines), with parameters as shown in table 1. (d) A_{cross} , (e) ζ_{cross} and (f) Ξ_{cross} , for $t = t_{max}(t_{inj}) = t_{inj}/(1 - \psi_{cross})$, with $t_{inj} \leq 0.01$, which are obtained, respectively, by equations (5.1)–(5.3) evaluated at ψ_{cross} (solid lines), and by equations (S7.5)–(S7.7) (dotted lines), with parameters as shown in table 1.

to decrease. By contrast, in figure 7d–f, we see A_{cross} , ζ_{cross} and Ξ_{cross} , respectively, decrease as time t increases. The implications of these findings for ζ_{cross} in particular are discussed next.

(c) Data for the corner’s vertical location

As shown in figure 7e, ζ_{cross} decreases with increasing t , which has an important implication: the vertical location of the concave corner is higher up in y than was predicted at leading order. Using equation (6.7) for the vertical location of the concave corner over time, along with data from table 1 fed into equation (S7.6), we can deduce

$$y_{2nd,cross} \approx 1 - 0.4698t + 0.0843t^2. \tag{7.3}$$

This is plotted in figure 8, representing an improvement over and above the formula $y_{1st,cross}$ given by equation (4.1) (also plotted in figure 8). In this same figure, we also show (obtained parametrically by varying t_{inj}) values computed for $y_{cross}^{inter} = 1 - (t_{inj}/2)\zeta_{+cross}$, as given by equation (6.6), versus $t = t_{max} \equiv t_{inj}/(1 - \psi_{cross}(t_{inj}))$ as given by equation (S2.2) in the electronic supplementary material. That this parametric expression for y_{cross}^{inter} versus t must agree well with equation (7.3) for sufficiently small t follows from the two curves as seen in figure 7e initially having the same slope. As t increases though (albeit well beyond the domain plotted in figure 7e) considerable deviation sets in between y_{cross}^{inter} and $y_{2nd,cross}$, and this is what we see in figure 8. This is mainly associated with the ζ_{+cross} values obtained within equation (6.6) falling well below the predictions of a small t_{inj} expansion given by equation (S7.2), ultimately leading to y_{cross}^{inter} values exceeding $y_{2nd,cross}$. Moreover, we plot an Eulerian-predicted position of the concave corner, a numerical result given by [32]

$$y_{Eulerian} = 1 - 0.4635t + 0.0784t^2, \tag{7.4}$$

obtained via interpolation of numerical data, fitted over a time domain $t \in [0, 2]$, in a space domain $x \in [0, 2]$, $y \in [0, 1]$, where the grid size for the solution variable in the numerical Eulerian

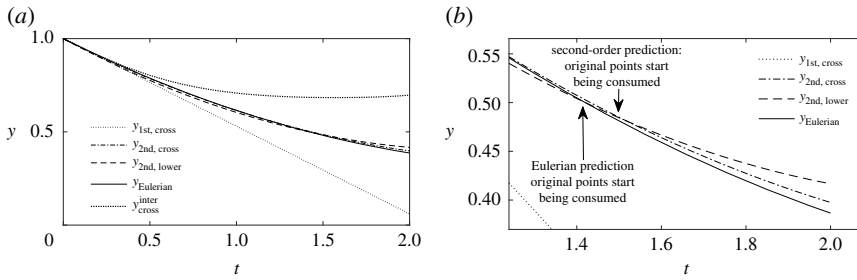


Figure 8. Vertical y position of the concave corner as a function of time t . (a) Dotted line: first-order solution $y_{1st,cross}$ given by equation (4.1). Dash-dotted line: second-order solution $y_{2nd,cross}$ given by equation (7.3). Dashed line: solution for a material point originally at the top of the lower region $y_{2nd,lower}$, see equation (2.12). Solid line: Eulerian numerical solution $y_{Eulerian}$, obtained in time domain $t \in [0, 2]$ with a grid spacing of $\Delta x = \Delta y = 2.5 \times 10^{-3}$, and Δt adjusted via Courant–Friedrichs–Lewy condition (CFL) condition [32]. Dense-dotted line: solution y_{cross}^{inter} given by equation (6.6). (b) Zoomed view of (a) at later times. We show via Eulerian versus via the current second-order prediction, the estimated point where material points originally on the front at time $t = 0$ start being consumed (at which $y_{2nd,lower}$ moves above the concave corner).

method [32] was $\Delta x = \Delta y = 2.5 \times 10^{-3}$, with the time step Δt set via the Courant–Friedrichs–Lewy condition (CFL) [34]. Over the domain in figure 8, these Eulerian data are evidently close to $y_{2nd,cross}$ data but further away from the data for y_{cross}^{inter} . We have also plotted the trajectory of the topmost point of the lower region $y_{2nd,lower}$ given by equation (2.12), via a second-order approximation (figure 8). By comparing $y_{2nd,lower}$ with the position of the concave corner obtained via our $y_{2nd,cross}$, we can determine that not only are material points from the upper region being consumed by the concave corner (which follows because $t_{inj(min)} = (1 - \psi_{cross})t$ is an increasing function of time), but also that material points must initially be extracted from the concave corner in order to populate the lower region, as early on $y_{2nd,lower}$ is below $y_{2nd,cross}$. This however only appears to happen until a certain time, after which points of the lower region start being consumed by the concave corner. Indeed at a certain time $y_{2nd,lower}$ intersects the concave corner (figure 8b): all extracted points have now been consumed. So, initially new points are extracted into the lower region, then those same points are consumed, after which the points originally present in the lower region start being consumed.

We have currently several different methods to estimate the position of the concave corner, hence different estimates of when $y_{2nd,lower}$ and the concave corner might coincide.

Via the first-order analytical solution for the corner $y_{1st,cross}$, compared to $y_{2nd,lower}$, we could determine that originally present points start being consumed by the concave corner from time $t \approx 0.289$ at $y \approx 0.864$, although this result is likely to be unreliable employing as it does $y_{1st,cross}$. Meanwhile the point y_{cross}^{inter} never coincides with $y_{2nd,lower}$ for any $t > 0$. However, the second-order solution for the corner $y_{2nd,cross}$ coincides with $y_{2nd,lower}$ at time $t \approx 1.518$ at $y \approx 0.481$. On the other hand, by using the corner location as predicted via the Eulerian method, we determine that material points originally present in the lower region start being consumed by the concave corner at time $t \approx 1.416$ at $y \approx 0.501$ (figure 8b). At the comparatively large times considered here, there is difference among the various predictions. The difference is unsurprising, since our first- and second-order analytical solutions are formally small time expansions, so we do not expect them to be valid all the way up to $t = 2$. To quantify deviations between the Eulerian data and the various other solutions that we have derived, we measure the root-mean-square (RMS) error with respect to the Eulerian data, up to $t = 2$. The RMS error between $y_{Eulerian}$ and $y_{1st,cross}$ turned out to be 0.1473, between $y_{Eulerian}$ and y_{cross}^{inter} it was 0.1518, and between $y_{Eulerian}$ and $y_{2nd,cross}$ it was 0.0039. This proves that the second-order solution given by equation (7.3) gives a much better estimate for the concave corner position over time than the first-order solution does, as expected. In addition, the RMS difference between $y_{Eulerian}$ and $y_{2nd,lower}$ was found to be 0.0118, which is larger than the error between $y_{Eulerian}$ and $y_{2nd,cross}$. The difference between $y_{Eulerian}$ and

$y_{2\text{nd,cross}}$ must come from either higher order corrections in time (and hence not captured within equations (5.1)–(5.3)) or by $y_{2\text{nd,cross}}$ or else truncation error in the numerical scheme used to obtain y_{Eulerian} . Since the difference between y_{Eulerian} and $y_{2\text{nd,lower}}$ is however larger than this, we assert that the difference between $y_{2\text{nd,lower}}$ and the location of the concave corner is genuine and not solely due to error in our second-order expansion. Thus, we confirm that we are actually extracting material points to populate the lower region at early times, but later on, we consume those extracted points again. However, doubt is still present, regarding the exact time at which material points originally present on the front start being consumed, as our estimates require extrapolation out of the $t \ll 1$ domain where second-order solutions formally apply.

In summary, we found that our second-order predicted location of the concave corner fits the Eulerian data reasonably well, at both small times $t \ll 1$ and also up to times of order unity. Nevertheless, for points away from the concave corner, we have not yet demonstrated whether the position of the Lagrangian material points forming the upper region fit front shape predictions from the Eulerian numerical data. This will be considered in the next section.

8. Second-order front shape at later times

To check reliability of our second-order results, we compute for a given time $t = 1$, the front shape $(-\mathcal{E}, -\zeta)$ (figure 9a), as a collection of material points with different t_{inj} all at the same t , specifically $t = 1$. Thus, we fix t and vary t_{inj} from $t_{\text{inj}(\text{min})}$ to t , by varying ψ , from 0 up to ψ_{cross} . We plot $(-\mathcal{E}, -\zeta)$ at both first order (equations (3.4)–(3.5)) and second order (equations (5.2)–(5.3)) comparing results with the numerical Eulerian data. When $t = 1$, the first-order theory predicts $t_{\text{inj}(\text{min})} = 1 - \psi_{\text{cross},0} \approx 0.0569$, whereas the second-order procedure (i.e. tracking (5.6)–(5.7) until they match with (5.8)) requires $t_{\text{inj}(\text{min})} \approx 0.0997$ to achieve matching at $t = 1$. This is already outside the domain $t_{\text{inj}} \in [0, 0.01]$ analysed in §7 and likewise outside the domain in which we can apply equation (7.2) to estimate t_{inj} given t . A value $t_{\text{inj}(\text{min})} \approx 0.0997$ when $t = 1$ implies $\psi_{\text{cross}} \approx 0.9003$ in order for equations (5.6)–(5.7) and (5.8) to match, which is actually less than the value of $\psi_{\text{cross},0}$. It follows that ψ_{cross} initially increases as t_{inj} increases (as per figure 5), but for large t_{inj} , it starts to decrease. In addition to front shape data $(-\mathcal{E}, -\zeta)$ as plotted in figure 9a, we also show, in figure 9b, the orientation angle A versus ζ . For the upper region, this is given parametrically, in terms of $A_0(\psi)$ and $\zeta_0(\psi)$ (at first order) and $A(\psi, t)$ and $\zeta(\psi, t)$ (at second order), via equations (3.3), (3.4), (5.1) and (5.2). We also plot the lower region angle $A(t)$ versus $\zeta(t)$, which is determined either using equation (2.1) (accurate to order $t^{3/2}$ in x) or else via (S3.6) (in the electronic supplementary material; accurate to order $t^{5/2}$ in x) coupled with equation (2.11). The upper and lower region predictions are compared with Eulerian data, although in figure 9b these display oscillations in the neighbourhood of the concave corner, which are just numerical artefacts [32]. In figure 9a, we see how the self-similar nature of ζ and \mathcal{E} , present at early times, is broken at a finite time $t = 1$. Here, we also appreciate how the upper region given by equations (5.2) and (5.3), intersects the lower region given by equation (5.4), at $\zeta(\psi_{\text{cross}}, t = 1) \approx 0.5839$ and $\mathcal{E}(\psi_{\text{cross}}, t = 1) \approx 0.1627$, with $\psi_{\text{cross}} \approx 0.9003$ (horizontal line labelled {1} in figure 9a). This point corresponds to a y value of $y_{\text{cross}}^{\text{inter}}$ at $t = 1$ (figure 8). Nevertheless, we extend the second-order solution via a linear extrapolation up to the point where equation (S7.6) would predict the location of the concave corner (see §S9 in the electronic supplementary material for details), suggesting instead $\zeta_{\text{cross}}(t = 1) \approx 0.7711$ (horizontal line labelled {2} in figure 9a). This now corresponds to a y value of $y_{2\text{nd,cross}}$ at $t = 1$ (figure 8). Here, we see also that our current second-order solution for ζ versus \mathcal{E} is closer to the Eulerian data than the first-order solution is. Indeed the dotted curve, corresponding to the upper region via a first-order approximation ($\zeta_0(\psi)$, $\mathcal{E}_0(\psi)$), finishes even further away, with $\zeta_{\text{cross},0} \approx 0.9397$ and $\mathcal{E}_{\text{cross},0} \approx 0.2733$ (values quoted in table 1; see the horizontal line labelled {3} in figure 9a corresponding to $y_{1\text{st,cross}}$ in figure 8), intercepting the lower region predicted by (4.1) (thick-dotted line). In addition, we see that the lower region (given by the second-order equation (5.4) at least for parts of the lower region near the concave corner), is relatively close to the Eulerian solution, more so than first-order equation (2.9). In figure 9b, we show the orientation angle A versus ζ , highlighting, as in figure 9a,

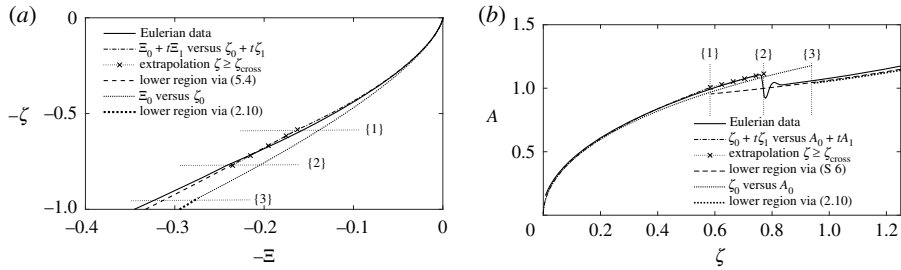


Figure 9. (a) Front shape $(-\mathcal{E}, -\zeta)$ at time $t = 1$, via first- and second-order solutions, for upper and lower regions, compared with Eulerian data. Solid line: Eulerian data. Dash-dotted line: second-order approximation $\zeta_0(\psi) + t\zeta_1(\psi)$ and $\mathcal{E}_0(\psi) + t\mathcal{E}_1(\psi)$ for the upper region, given by equations (5.2) and (5.3), respectively, up to intersection with the lower region (dashed line) computed via equation (5.4). At time $t = 1$, the intersection occurs at $\zeta(\psi_{\text{cross}}) \approx 0.5839$ with $\mathcal{E}(\psi_{\text{cross}}) \approx 0.1627$, horizontal line labelled {1}. We have however computed ζ versus \mathcal{E} further than this ‘x’ line; see §S9 in the electronic supplementary material for details), up to a ζ value obtained by extrapolating the prediction of equation (S7.6) up to $t = 1$, which gives $\zeta_{\text{cross}}(t = 1) \approx 0.7711$ (horizontal line labelled {2}), with a corresponding value of $\mathcal{E} \approx 0.2353$ (this value is slightly different from that predicted by extrapolation of equation (S7.7), which gives instead $\mathcal{E}_{\text{cross}}(t = 1) \approx 0.2476$). Dotted line: first-order approximation $\zeta_0(\psi)$ and $\mathcal{E}_0(\psi)$ for the upper region, given by equations (3.4) and (3.5), up to the intersection with the lower region via equation (2.9) (thick-dotted line), with $\zeta_{\text{cross},0} \approx 0.9397$ and $\mathcal{E}_{\text{cross},0} \approx 0.2733$ (horizontal line labelled {3}). (b) Rescaled front orientation angle A versus rescaled vertical coordinate ζ . Solid line: Eulerian data. Dash-dotted line: second-order approximation $A_0(\psi) + tA_1(\psi)$ and $\zeta_0(\psi) + t\zeta_1(\psi)$ for the upper region, given by equations (5.1) and (5.2), computed at time $t = 1$ up to the intersection with the lower region (given by equation (5.4)), which occurs at $A(\psi_{\text{cross}}) \approx 1.0063$ with $\zeta(\psi_{\text{cross}}) \approx 0.5839$ (vertical line labelled {1}), with $\psi_{\text{cross}} \approx 0.9003$. We have however computed A versus ζ further than this ‘x’ line; see §S9 in the electronic supplementary material for details), up to a value of ζ (vertical line labelled {2}) obtained as before by extrapolating equation (S7.6), $\zeta_{\text{cross}}(t = 1) \approx 0.7711$, and a corresponding value of $A \approx 1.1131$ (note that this value is slightly different from that predicted by extrapolation of equation (S7.5), which gives $A_{\text{cross}}(t = 1) \approx 1.1259$). Here, we can also see the lower region computed via equation (5.4) (dashed line) obtained for $\zeta \geq \zeta(\psi_{\text{cross}}) \approx 0.5839$, i.e. starting from the vertical line labelled {1}. Dotted line: first-order approximation $A_0(\psi)$ and $\zeta_0(\psi)$ for the upper region, given by equations (3.3) and (3.4), respectively. Thick-dotted line: lower region computed via equation (2.1), for $\zeta > \zeta_{\text{cross},0}$ (vertical line labelled {3}). We see that {2} agrees better with the Eulerian prediction of the corner location than {1} does.

the second-order matching procedure (vertical line labelled {1} in figure 9b, corresponding to $y_{\text{cross}}^{\text{inter}}$), data extended up to the concave corner location predicted by equation (S7.6) (vertical line labelled {2} in figure 9b, corresponding to $y_{2\text{nd,cross}}$), and we also show the intersection between the two regions via the first-order solution (vertical line labelled {3} in figure 9b, corresponding to $y_{1\text{st,cross}}$). The value of $A(\psi_{\text{cross}}) \approx 1.0063$ (labelled {1}) in figure 9b is curious. This is so close to unity that the orientation of the upper and lower regions is nearly parallel, making it possible in figure 9a to extrapolate the solution of the upper region and still remain close to the lower region. In a near parallel case like that it is difficult to pinpoint exactly where the intersection between these regions occurs. This may help to explain why the Eulerian prediction seems to give the concave corner (with a sudden decrease of A in figure 9b) at a different ζ value, closer to the point labelled {2} than {1}: we already know from figure 8 that $y_{2\text{nd,cross}}$ fits y_{Eulerian} better than $y_{\text{cross}}^{\text{inter}}$ does. Despite the subtleties, from figure 9a,b, we see that the current second-order solution fits the Eulerian data better than the first-order solution does, giving good agreement even up to times of order unity.

9. Conclusion

We have considered a dimensionless form of the pressure-driven growth model used to predict the foam front propagation in an oil reservoir. The front has been captured as the region of finely textured foam of very low mobility, where injected gas meets reservoir liquid. The foam front

is represented as a curve of negligible thickness, which propagates through the porous medium due to the pressure difference across it and at the same time is retarded by dissipation. The focus here was on early time behaviour, such that the distance the front has propagated horizontally is less than the maximum vertical depth through which it can displace, albeit some of the results we present are extrapolated beyond that regime. As was shown in previous studies [27,32], the foam front can be divided vertically into two regions (lower and upper) that intersect in a concave corner. In this study, we have obtained a second-order solution in time to track the trajectory of the material points of the upper region of the front, up to the aforementioned concave corner or matching point between both regions. Obtaining the second-order solution in the upper region was particularly challenging owing to strong spatio-temporal non-uniformities that are present there. Our approach was to start with solutions in terms of dimensionless similarity solutions, but then at second order include corrections showing how those similarity solutions break down. This obtained an approximation accurate to order $t^{5/2}$ for the horizontal x location of the material points of the upper region of the front, and an order t^2 accurate approximation for their vertical y location, in each case, with the same order at which the lower region has been computed. At any specified time t , a second-order solution predicted the vertical location of the concave corner higher up than the first-order solution, but very close to the prediction of an independently obtained Eulerian prediction. We have also proven that initially material points are extracted from the concave corner to populate the lower region, since the topmost point originally present on the front at time $t = 0$ initially moves down faster than the concave corner does, as predicted via the first- and/or second-order solution obtained in this study. Later on, due to second-order effects in time, with the downward motion of such material points slowing down over time, the lower region material points originally on the front eventually reach the concave corner, which must therefore have consumed any previously extracted material points. Therefore, we can assert that all points extracted into the lower region are eventually consumed, however, based on the different approximations that we use, we can actually have different predictions for exactly when this occurs. The issue is that the time we are trying to identify is already sufficiently long that there might be some uncertainty whether expanding in time as far as a second-order solution remains adequate or whether yet a higher order correction is required, which will be challenging in view of strong spatio-temporal non-uniformities present in the upper region. Nevertheless, with the new solutions, we were also able to compute the shape of the upper region of the front, which fitted the Eulerian data even up to times of order unity.

Data accessibility. All results presented here are analytically reproducible, as detailed in the article and in the electronic supplementary material.

Authors' contributions. P.G. conceived the research problem and suggested it to C.T.-U. to tackle as part of C.T.-U.'s PhD project. C.T.-U. executed the study and drafted the article, with P.G. performing a critical revision of the draft article and providing feedback. This drafting and revision process was then iterated between P.G. and C.T.-U. through a further 10 drafts. Both authors approved the final version and agree to be accountable for all aspects of the work.

Competing interests. We declare we have no competing interests.

Funding. C. T.-U. received ANID Becas-Chile funding.

Acknowledgements. C. T.-U. acknowledges useful conversations with E. Mas-Hernández and Y. A. Boakye-Ansah.

References

1. Stevenson P. 2012 *Foam engineering: fundamentals and applications*. Oxford, UK: John Wiley & Sons.
2. Drenckhan W, Cox SJ, Delaney G, Holste H, Weaire D, Kern N. 2005 Rheology of ordered foams: on the way to discrete microfluidics. *Colloids Surf. A* **263**, 52–64. (doi:10.1016/j.colsurfa.2005.01.005)
3. Kotb MM, Shakiban HK, Sawaby AF. 2013 Foam treatment for varicose veins: efficacy and safety. *Alexandria J. Med.* **49**, 249–253. (doi:10.1016/j.ajme.2012.11.003)
4. Lake LW. 1989 *Enhanced Oil Recovery*. Englewood Cliffs, NJ: Prentice Hall.

5. Shan D, Rossen WR. 2004 Optimal injection strategies for foam IOR. *SPE J.* **9**, 132–150. (doi:10.2118/75180-MS)
6. Wang S, Mulligan CN. 2004 An evaluation of surfactant foam technology in remediation of contaminated soil. *Chemosphere* **57**, 1079–1089. (doi:10.1016/j.chemosphere.2004.08.019)
7. Géraud B, Jones SA, Cantat I, Dollet B, Méheust Y. 2016 The flow of a foam in a two-dimensional porous medium. *Water Resour. Res.* **52**, 773–790. (doi:10.1002/2015WR017936)
8. Shen X, Zhao L, Ding Y, Liu B, Zeng H, Zhong L, Li X. 2011 Foam, a promising vehicle to deliver nanoparticles for vadose zone remediation. *J. Hazard. Mater.* **186**, 1773–1780. (doi:10.1016/j.jhazmat.2010.12.071)
9. Zhong L, Szecsody JE, Zhang F, Mattigod SV. 2010 Foam delivery of amendments for vadose zone remediation: propagation performance in unsaturated sediments. *Vadose Zone J.* **9**, 757–767. (doi:10.2136/vzj2010.0007)
10. Grassia P, Mas-Hernández E, Shokri N, Cox SJ, Mishuris G, Rossen WR. 2014 Analysis of a model for foam improved oil recovery. *J. Fluid Mech.* **751**, 346–405. (doi:10.1017/jfm.2014.287)
11. Ma K, Lopez-Salinas JL, Puerto MC, Miller CA, Biswal SL, Hirasaki GJ. 2013 Estimation of parameters for the simulation of foam flow through porous media. Part 1: the dry-out effect. *Energy Fuels* **27**, 2363–2375. (doi:10.1021/ef302036s)
12. Kovscek AR, Bertin HJ. 2003 Foam mobility in heterogeneous porous media. I. Scaling concepts. *Transp. Porous Media* **52**, 17–35. (doi:10.1023/A:1022312225868)
13. Khatib ZI, Hirasaki GJ, Falls AH. 1988 Effects of capillary pressure on coalescence and phase mobilities in foams flowing through porous media. *SPE Reservoir Eng.* **3**, 919–926. (doi:10.2118/15442-PA)
14. Bera A, Ojha K, Mandal A. 2013 Synergistic effect of mixed surfactant systems on foam behavior and surface tension. *J. Surfactants Deterg.* **16**, 621–630. (doi:10.1007/s11743-012-1422-4)
15. Osei-Bonsu K, Shokri N, Grassia P. 2016 Fundamental investigation of foam flow in a liquid-filled Hele-Shaw cell. *J. Colloid Interface Sci.* **462**, 288–296. (doi:10.1016/j.jcis.2015.10.017)
16. Kumar S, Mandal A. 2017 Investigation on stabilization of CO₂ foam by ionic and nonionic surfactants in presence of different additives for application in enhanced oil recovery. *Appl. Surf. Sci.* **420**, 9–20. (doi:10.1016/j.apsusc.2017.05.126)
17. Osei-Bonsu K, Grassia P, Shokri N. 2017 Relationship between bulk foam stability, surfactant formulation and oil displacement efficiency in porous media. *Fuel* **203**, 403–410. (doi:10.1016/j.fuel.2017.04.114)
18. Osei-Bonsu K, Grassia P, Shokri N. 2017 Investigation of foam flow in a 3D printed porous medium in the presence of oil. *J. Colloid Interface Sci.* **490**, 850–858. (doi:10.1016/j.jcis.2016.12.015)
19. Hirasaki G, Lawson J. 1985 Mechanisms of foam flow in porous media: apparent viscosity in smooth capillaries. *Soc. Petroleum Eng. J.* **25**, 176–190. (doi:10.2118/12129-PA)
20. Ma K, Mateen K, Ren G, Luo H, Bourdarot G, Morel D. 2018 Mechanistic modeling of foam flow through porous media in the presence of oil: review of foam-oil interactions and an improved bubble population-balance model. *SPE Annual Technical Conference and Exhibition, Dallas, TX, 24–26 September*. (doi:10.2118/191564-MS)
21. Mas-Hernández E, Grassia P, Shokri N. 2015 Foam improved oil recovery: foam front displacement in the presence of slumping. *Colloids Surf. A* **473**, 123–132. (doi:10.1016/j.colsurfa.2014.12.023)
22. Ma K, Ren G, Mateen K, Morel D, Cordelier P. 2015 Modeling techniques for foam flow in porous media. *SPE J.* **20**, 453–470. (doi:10.2118/169104-PA)
23. Eneotu M, Grassia P. 2020 Modelling foam improved oil recovery: towards a formulation of pressure-driven growth with flow reversal. *Proc. R. Soc. A: Math., Phys. Eng. Sci.* **476**, 2020–0573. (doi:10.1098/rspa.2020.0573)
24. Kovscek AR, Patzek TW, Radke CJ. 1995 A mechanistic population balance model for transient and steady-state foam flow in Boise sandstone. *Chem. Eng. Sci.* **50**, 3783–3799. (doi:10.1023/A:1010740811277)
25. Falls AH, Hirasaki GJ, Patzek TW, Gauglitz DA, Miller DD, Ratulowski T. 1988 Development of a mechanistic foam simulator: the population balance and generation by snap-off. *SPE Reservoir Eng.* **3**, 884–892. (doi:10.2118/14961-PA)
26. Farajzadeh R, Andrianov A, Krastev R, Hirasaki GJ, Rossen WR. 2012 Foam–oil interaction in porous media: implications for foam assisted enhanced oil recovery. *Adv. Colloid Interface Sci.* **183–184**, 1–13. (doi:10.1016/j.cis.2012.07.002)

27. Grassia P, Lue L, Torres-Ulloa C, Berres S. 2017 Foam front advance during improved oil recovery: similarity solutions at early times near the top of the front. *J. Fluid Mech.* **828**, 527–572. (doi:10.1017/jfm.2017.541)
28. Salazar Castillo RO, Ter Haar SF, Ponnens CG, Bos M, Rossen W. 2020 Fractional-flow theory for non-Newtonian surfactant-alternating-gas foam processes. *Transp. Porous Media* **131**, 399–426. (doi:10.1007/s11242-019-01351-6)
29. Kovscek AR, Patzek TW, Radke CJ. 1997 Mechanistic foam flow simulation in heterogeneous and multidimensional porous media. *SPE J.* **2**, 511–526. (doi:10.2118/39102-PA)
30. Zeng Y *et al.* 2016 Insights on foam transport from a texture-implicit local-equilibrium model with an improved parameter estimation algorithm. *Ind. Eng. Chem. Res.* **55**, 7819–7829. (doi:10.1021/acs.iecr.6b01424)
31. Mas Hernández E, Grassia P, Shokri N. 2016 Modelling foam improved oil recovery within a heterogeneous reservoir. *Colloids Surf. A* **510**, 43–52. (doi:10.1016/j.colsurfa.2016.07.064)
32. Torres-Ulloa C, Berres S, Grassia P. 2018 Foam-liquid front motion in Eulerian coordinates. *Proc. R. Soc. A* **474**, 20180290. (doi:10.1098/rspa.2018.0290)
33. Kurganov A, Noelle S, Petrova G. 2001 Semidiscrete central-upwind schemes for hyperbolic conservation laws and Hamilton–Jacobi equations. *SIAM J. Sci. Comput.* **23**, 707–740. (doi:10.1137/S1064827500373413)
34. Osher S, Fedkiw R. 2006 *Level set methods and dynamic implicit surfaces*. Berlin, Germany and London, UK: Springer. (doi:10.1007/b98879)
35. Grassia P, Torres-Ulloa C, Berres S, Mas-Hernández E, Shokri N. 2016 Foam front propagation in anisotropic oil reservoirs. *Eur. Phys. J. E* **39**, 42 (doi:10.1140/epje/i2016-16042-5)
36. de Velde Harsenhorst RM, Dharma AS, Andrianov A, Rossen WR. 2014 Extension of a simple model for vertical sweep in foam SAG displacements. *SPE Reservoir Eval. Eng.* **17**, 373–383. (doi:10.2118/164891-PA)
37. Chan TF, Vese LA. 2001 Active contours without edges. *IEEE Trans. Image Process.* **10**, 266–277. (doi:10.1109/83.902291)